



1 **Optimizing sampling strategies in high-resolution paleoclimate records**

2

3 Niels J. de Winter^{1,2} *, Tobias Agterhuis¹, Martin Ziegler¹

4

5 ¹Department of Earth Sciences, Utrecht University, Princetonlaan 8a, 3584 CB Utrecht, the Netherlands

6 ²AMGC research group, Vrije Universiteit Brussel, Pleinlaan 2, 1050 Brussels, Belgium

7

8 Correspondence to: Niels J. de Winter (n.j.dewinter@uu.nl)

9



10 **Abstract**

11 The aim of paleoclimate studies to resolve climate variability from noisy proxy records can in essence be
12 reduced to a statistical problem. The challenge is to isolate meaningful information on climate events from
13 these records by reducing measurement uncertainty through a combination of proxy data while retaining
14 the temporal resolution needed to assess the timing and duration of the event. In this study, we explore the
15 limits of this compromise by testing different methods for combining proxy data (smoothing, binning and
16 sample size optimization) on a particularly challenging paleoclimate problem: resolving seasonal variability
17 in stable isotope records. We test and evaluate the effects of changes in the seasonal temperature and
18 hydrology cycle as well as changes in accretion rate of the archive and parameters such as sampling
19 resolution and age model uncertainty on the reliability of seasonality reconstructions based on clumped and
20 oxygen isotope analyses in 33 real and virtual datasets. Our results show that strategic combinations of
21 clumped isotope analyses can significantly improve the accuracy of seasonality reconstructions if compared
22 with conventional stable oxygen isotope analyses, especially in settings where the isotopic composition of
23 the water is poorly constrained. Smoothing data using a moving average often leads to a dampening of the
24 seasonal cycle, significantly reducing the accuracy of reconstructions. A statistical sample size optimization
25 protocol yields more precise results than smoothing. However, the most accurate results are obtained
26 through monthly binning of proxy data, especially in cases where growth rate or water composition cycles
27 dampen the seasonal temperature cycle. Our analysis of a wide range of natural situations reveals that the
28 effect of temperature seasonality on isotope records almost invariably exceeds that of changes in water
29 composition. Thus, in most cases, isotope records allow reliable identification of growth seasonality as a
30 basis for age modelling and seasonality reconstructions in absence of independent chronological markers
31 in the record. These specific findings allow us to formulate general recommendations for sampling and
32 combining data in paleoclimate research and have implications beyond the reconstruction of seasonality.
33 We discuss the implications of our results for solving common problems in paleoclimatology and
34 stratigraphy, including cyclostratigraphy, strontium isotope dating and event stratigraphy.

35



36 **1. Introduction**

37 Improving the resolution of climate reconstructions is a key objective in paleoclimate studies because it
38 allows climate variability to be studied on different timescales and sheds light on the continuum of climate
39 variability (Huybers and Curry, 2006). However, the temporal resolution of climate records is limited by the
40 accretion rate (growth or sedimentation rate) of the archive and the spatial resolution of sampling for climate
41 reconstructions, which is a function of the size of samples required for a given climate proxy. This tradeoff
42 between sample size and sampling resolution is especially prevalent when using state-of-the-art climate
43 proxies which require large sample sizes, such as the carbonate clumped isotope paleothermometer (Δ_{47} ;
44 see applications in Rodríguez-Sanz et al., 2017; Briard et al., 2020) or stable isotope ratios in specific
45 compounds or of rare isotopes (e.g. phosphate-oxygen isotopes in tooth apatite, triple oxygen isotopes in
46 speleothems or carbon isotopes of CO₂ in ice cores; Jones et al., 1999; Schmitt et al., 2012; Sha et al.,
47 2020). The challenge of sampling resolution persist on a wide range of timescales: from attempts to resolve
48 geologically short-lived (kyr-scale) climate events from deep sea cores with low sedimentation rates (e.g.
49 Stap et al., 2010; Rodríguez-Sanz et al., 2017) to efforts to characterize tidal or daily variability in
50 accretionary carbonate archives (e.g. Warter and Müller, 2017; de Winter et al., 2020a). What constitutes
51 “high-resolution” is therefore largely dependent on the specifics of the climate archive.

52 Sample size limitations are especially important in paleoseasonality reconstructions. Reliable archives for
53 seasonality (e.g. corals, mollusks and speleothem records) are in high demand in the paleoclimate
54 community, because the seasonal cycle is the most important cycle in Earth’s climate and seasonality
55 reconstructions complement more common long-term (kyr to -Myr) records of past climate variability (e.g.
56 Morgan and van Ommen, 1997; Tudhope et al., 2001; Steuber et al., 2005; Steffensen et al., 2008; Denton
57 et al., 2005; Huyghe et al., 2015; Vansteenberghe et al., 2019). A more detailed understanding of climate
58 dynamics at the human timescale is increasingly relevant for improving climate projections (IPCC, 2013).
59 Unfortunately, the growth and mineralization rates of archives that capture high-resolution variability (rarely
60 exceeding 10 mm/yr) limit the number and size of samples that can be obtained at high temporal resolutions
61 (e.g. Mosley-Thompson et al., 1993; Passey and Cerling, 2002; Treble et al., 2003; Goodwin et al., 2003).



62 A promising technique for circumventing sample size limitations is to analyze larger numbers of small
63 aliquots from the same sample or from similar parts of the climate archive. These smaller aliquots typically
64 have a poorer precision, but averaging multiple aliquots into one estimate while propagating the
65 measurement uncertainty leads to a more reliable estimate of the climate variable (Dattalo, 2008; Meckler
66 et al., 2014; Müller et al., 2017; Fernandez et al., 2017). This approach yields improved sampling flexibility
67 since aliquots can be combined in various ways after measurement. It also allows outlier detection at the
68 level of individual aliquots, thereby spreading the risk of instrumental failure and providing improved control
69 on changes in measurement conditions that may bias results.

70 Previous studies have applied several different methods for combining data from paleoclimate records to
71 reduce analytical noise or higher order variability, and extract variability with a specific frequency (e.g. a
72 specific orbital cycle or seasonality; e.g. Lisiecki and Raymo, 2004; Cramer et al., 2009). These data
73 reduction approaches can in general be categorized into: **smoothing** techniques, in which a sliding window
74 or range of neighboring datapoints is used to smooth high resolution records (see e.g. Cramer et al., 2009)
75 or **binning** techniques, in which the record is divided into equal bins along its length axis (e.g. time, depth
76 or length in growth direction; e.g. Lisiecki and Raymo, 2004). In addition, a third approach is proposed here
77 based on **optimization** of sample size for dynamic binning of data along the climate cycle using a moving
78 window in the domain of the climate variable (as opposed to the depth domain) combined with a T-test
79 routine (see section 3.4). All three approaches have advantages and caveats.

80

81 **2. Aim**

82 In this study, we explore the (dis)advantages of these three data reduction approaches by testing their
83 reliability in resolving seasonal variability in sea surface temperature (SST) and seawater stable oxygen
84 isotope composition ($\delta^{18}\text{O}_{\text{sw}}$), both highly sought-after variables in paleoclimate research. We compare
85 reconstructions of SST and $\delta^{18}\text{O}_{\text{sw}}$ in real and virtual datasets from accretionary carbonate archives (e.g.
86 shells, corals and speleothems) using the clumped isotope thermometer (Δ_{47}) combined with stable oxygen
87 isotope ratios of the carbonate ($\delta^{18}\text{O}_{\text{c}}$). Throughout the remainder of this work, the three methods for
88 combining data for reconstructions are abbreviated as follows (see also **Fig. 1** and 3.4):



89 **Smoothing:** Reconstructions of SST and $\delta^{18}\text{O}_{\text{sw}}$ based on **moving averages** of Δ_{47} records.

90 **Binning:** Reconstructions of SST and $\delta^{18}\text{O}_{\text{sw}}$ based on binning of Δ_{47} records into **monthly time bins**.

91 **Optimization** Reconstructions of SST and $\delta^{18}\text{O}_{\text{sw}}$ based on **sample size optimization** in Δ_{47} records.

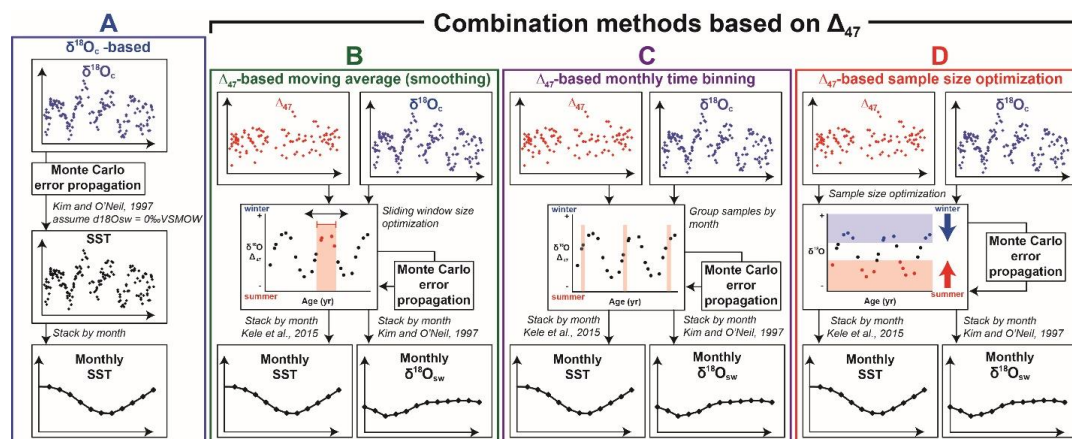
92 For comparison, we also include reconstructions based purely on individual $\delta^{18}\text{O}_{\text{c}}$ measurements with an
93 (often inaccurate) assumption of constant $\delta^{18}\text{O}_{\text{sw}}$, which form the most common method for carbonate-
94 based temperature reconstructions in paleoclimate research. These reconstructions were not subject to
95 any of the data combination methods outlined above and mostly serve as a benchmark to compare with
96 the performance of the Δ_{47} methods. SST reconstructions assuming constant $\delta^{18}\text{O}_{\text{sw}}$ are hereafter referred
97 to as “ $\delta^{18}\text{O}$ ” reconstructions.

98 We evaluate the reliability of all four approaches through measures of accuracy (offset of reconstruction
99 from the true value) and precision (variability between reconstructions due to random errors in the data) of
100 reconstructions and highlight biases inherent to specific approaches and in specific situations. In the end,
101 we provide guidelines for choosing the right sampling approach for studies on seasonality reconstructions
102 from accretionary carbonate archives. In addition, we discuss implications of our findings for other sampling
103 problems in the geosciences.

104



105



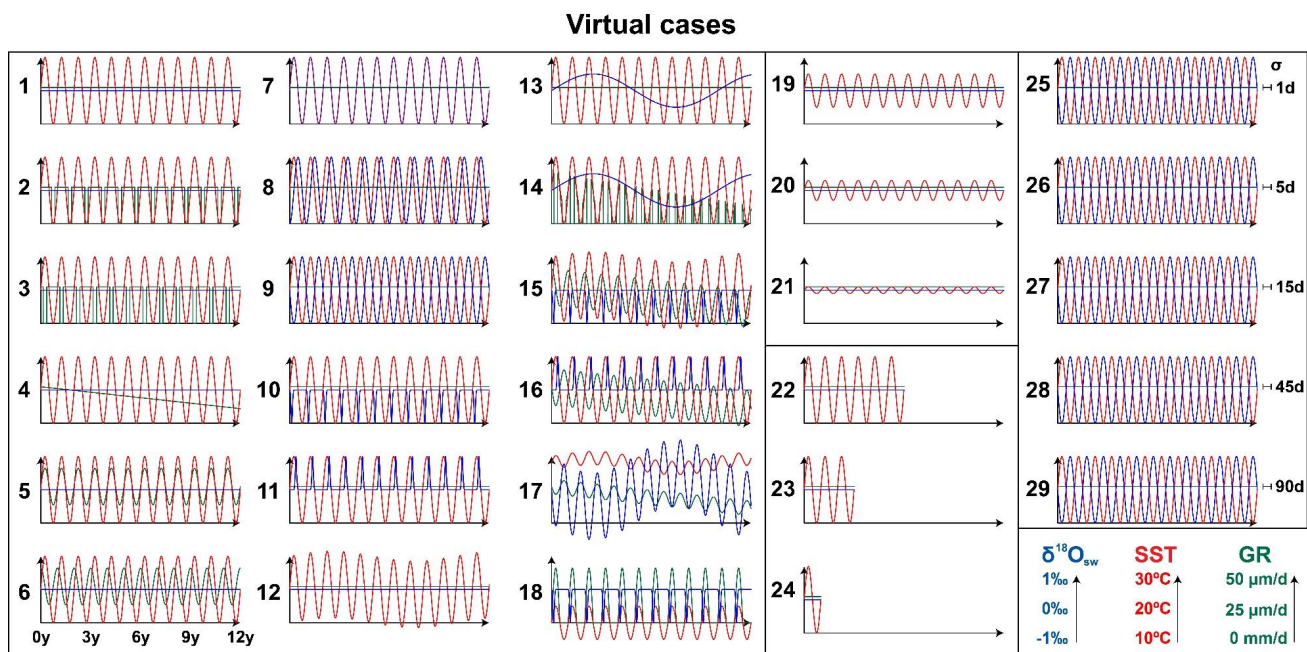
106 **Figure 1:** Schematic overview of the four approaches for seasonality reconstructions: (A) $\delta^{18}\text{O}$ -based
 107 reconstructions, assuming constant $\delta^{18}\text{O}_{\text{sw}}$. (B) Reconstructions based on **smoothing** $\delta^{18}\text{O}_c$ and Δ_{47} data
 108 using a moving average. (C) Reconstructions based on binning $\delta^{18}\text{O}_c$ and Δ_{47} data in monthly time bins.
 109 (D) Reconstructions based on **optimization** of the sample size for combining $\delta^{18}\text{O}_c$ and Δ_{47} data (see
 110 description in 3.4). Colored curves represent virtual $\delta^{18}\text{O}_c$ (blue) and Δ_{47} (red) depth series. Black curves
 111 represent reconstructed monthly SST and $\delta^{18}\text{O}_{\text{sw}}$ averages.

112

113 3. Methods

114 3.1 SST and $\delta^{18}\text{O}_{\text{sw}}$ data

115 The reliability (accuracy and precision) of approaches was illustrated and tested in three ways: Firstly, by
 116 evaluating data from a real specimen of a Pacific oyster (*Crassostrea gigas*, syn. *Magallana gigas*) reported
 117 in Ullmann et al. (2010). Secondly, by application on data based on actual measurements of natural
 118 variability in SST and sea surface salinity (SSS; case 30-33). Thirdly, by applying the approaches on set of
 119 virtual datasets based on completely virtual SST and $\delta^{18}\text{O}_{\text{sw}}$ data (case 1-29). For virtual datasets, records
 120 of SST and $\delta^{18}\text{O}_{\text{sw}}$ were converted to the depth domain (along the length of the record) by defining a virtual
 121 growth rate in the sampling direction. Adding this growth rate as a variable allowed us to test the sensitivity
 122 of approaches to changes in the extension rate of the archive, including hiatuses (growth rate = 0). This is
 123 important, because fluctuations in linear extension rate and periods in which no mineralization occurs
 124 (hiatuses or growth cessations) are common in all climate archives (e.g. Treble et al., 2003; Ivany, 2012).
 125 An overview of the virtual SST and $\delta^{18}\text{O}_{\text{sw}}$ time series in all test cases is shown in **Fig. 2** and a description
 126 of all cases is given in **S1**.



128 **Figure 2:** Overview of time series of all virtual test cases. Colored curves represent time series of SST (red), $\delta^{18}\text{O}_{\text{sw}}$ (blue) and growth rate (green,
 129 abbreviated as "GR"). Horizontal axes in all plots are 12 years long (see legend below case 6). Vertical axis of all plots has the same scale (SST:
 130 10 to 30°C; $\delta^{18}\text{O}_{\text{sw}}$: -1 to +1‰VSMOW; Growth rate: 0–50 $\mu\text{m}/\text{day}$; see legend in bottom right corner). Horizontal error bars and labels on the right
 131 side of cases 25–29 represent standard errors introduced on the age model (bars not to scale). The $\delta^{18}\text{O}_c$ and Δ_{47} records resulting from these virtual
 132 datasets are provided in **S8** (see also **Fig. 3** for natural examples).



133 2.1.1 Modern oyster data

134 Environmental SST and $\delta^{18}\text{O}_{\text{sw}}$ data from the List Basin in Denmark ($54^{\circ}59.25\text{N}$, $8^{\circ}23.51\text{E}$) where the
135 modern oyster specimen originated were obtained from local *in situ* measurements of SST and SSS
136 described in Ullmann et al. (2010). Since direct, *in situ* measurements of $\delta^{18}\text{O}_{\text{sw}}$ variability at a high temporal
137 resolution were not available, $\delta^{18}\text{O}_{\text{sw}}$ was estimated from (more widely available) SSS data using a mass
138 balance (equation 1 and 2; following e.g. Ullmann et al., 2010):

$$139 \quad \delta^{18}\text{O}_{\text{sw}} = \delta^{18}\text{O}_{\text{sw},\text{freshwater}} * f + \delta^{18}\text{O}_{\text{sw},\text{ocean}} * (1 - f) \quad (1)$$

$$140 \quad f = \frac{\text{SSS}_{\text{sample}} - \text{SSS}_{\text{ocean}}}{\text{SSS}_{\text{freshwater}} - \text{SSS}_{\text{ocean}}} \quad (2)$$

141 Here, we assume salinity ($\text{SSS}_{\text{sample}}$) results from a mixture of a fraction (f) isotopically light and low-salinity
142 ($\delta^{18}\text{O}_{\text{sw},\text{freshwater}} = -8.5\text{‰VSMOW}$; $\text{SSS}_{\text{freshwater}} = 0$) freshwater and a fraction ($1-f$) ocean water ($\delta^{18}\text{O}_{\text{sw},\text{ocean}}$
143 $= 0\text{‰VSMOW}$; $\text{SSS}_{\text{ocean}} = 35$), with negative amounts of freshwater contribution ($f < 0$) representing net
144 evaporation ($\text{SSS}_{\text{sample}} > \text{SSS}_{\text{ocean}}$). The value for $\delta^{18}\text{O}_{\text{sw},\text{freshwater}}$ was based on the discharge weighted
145 average $\delta^{18}\text{O}_{\text{sw}}$ of water in the nearby Elbe and Weser rivers (-8.5‰VSMOW ; see Ullmann et al., 2010).

146 3.1.2 Cases based on real climate data

147 Natural environmental time series were based on SST and SSS data from four different locations, selected
148 to capture a variety of environments with different SST and SSS variability:

- 149 1. Tidal flats of the Wadden Sea near Texel, the Netherlands (case 30)
- 150 2. Great Barrier Reef in Australia (case 31)
- 151 3. Gulf of Aqaba between Egypt and Saudi Arabia (case 32)
- 152 4. Northern Atlantic Ocean east of Iceland (case 33).

153 Daily measurements of SST and SSS for case 31-33 were obtained from worldwide open-access datasets
154 of the National Oceanic and Atmospheric Administration (NOAA, 2020) and European Space Agency (ESA,
155 2020) respectively. Hourly SST and SSS measured *in situ* in the Wadden Sea (case 30) were obtained
156 from the Dutch Institute for Sea Research (NIOZ, Texel, the Netherlands). Since direct, *in situ*
157 measurements of $\delta^{18}\text{O}_{\text{sw}}$ variability at a high temporal resolution is scarce, $\delta^{18}\text{O}_{\text{sw}}$ was estimated from (more

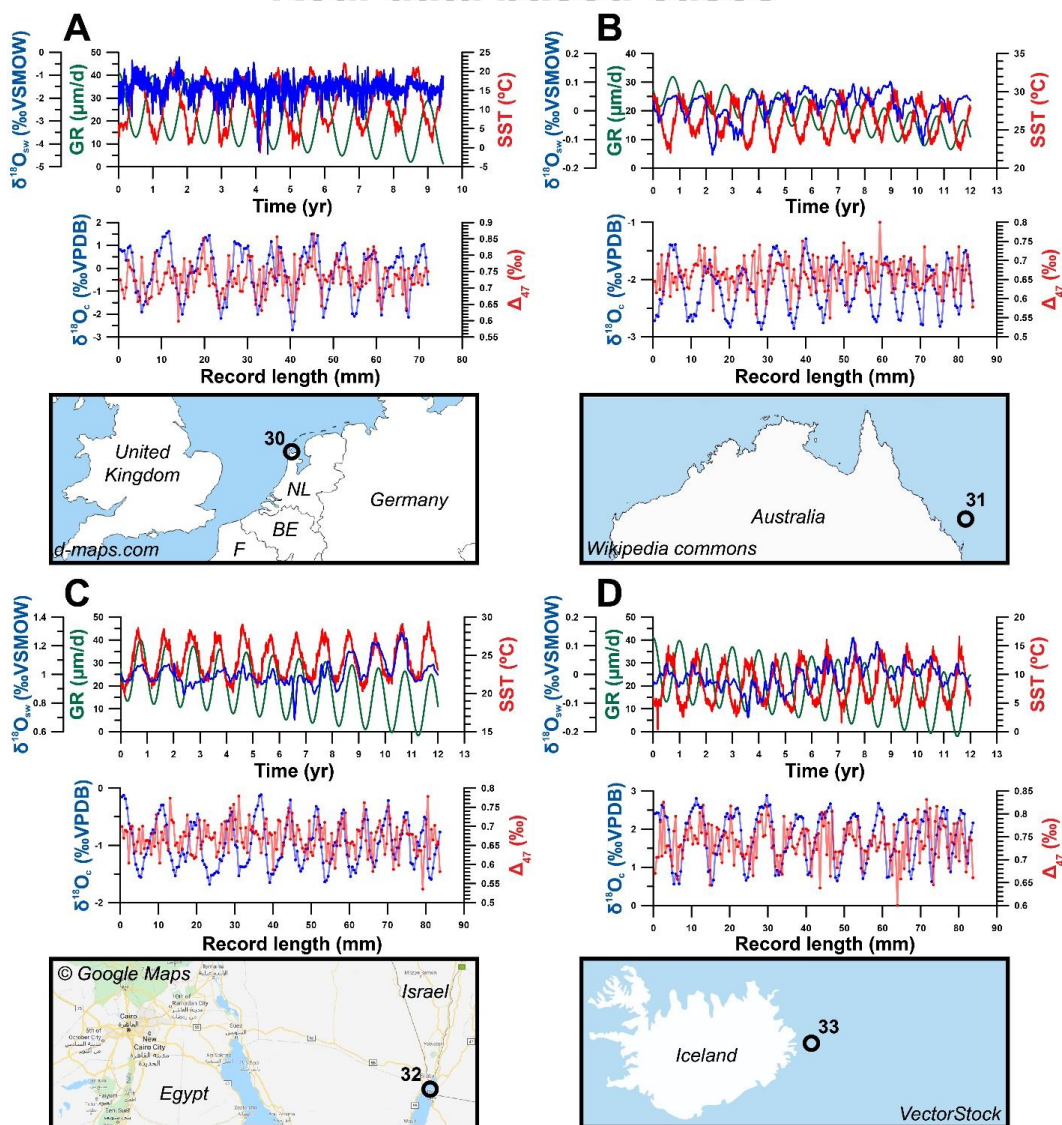


158 widely available) SSS data using the same mass balance described in **3.1.1**. The value for $\delta^{18}\text{O}_{\text{sw, freshwater}}$
159 was based on the $\delta^{18}\text{O}_{\text{sw}}$ of rain in the Netherlands (-8‰VSMOW ; Mook, 1970; Bowen, 2020), and applying
160 this mass balance on the SSS record of the Wadden Sea tidal flats (case 30) results in $\delta^{18}\text{O}_{\text{sw}}$ values and
161 a SSS- $\delta^{18}\text{O}_{\text{sw}}$ relationship in agreement with measurements in this region (Harwood et al., 2008). SST and
162 $\delta^{18}\text{O}_{\text{sw}}$ time series for all cases are given in **S5** and natural cases are plotted in **Fig. 3**.

163



Real data based cases



164

165 **Figure 3:** Overview of the four cases of virtual data based on natural SST and SSS measurements explored
 166 in this study. (A) Case 30: Tidal flats on the Wadden Sea, Texel, the Netherlands. (B) Case 31 Great Barrier
 167 Reef, Australia). (C) Case 32: Gulf of Aqaba between Egypt and Saudi Arabia. (D) Case 33: Atlantic Ocean
 168 east of Iceland. For all cases, graphs on top show environmental data, with SST plotted in red, $\delta^{18}O_{sw}$ in
 169 blue and growth rate (abbreviated as "GR") in green (as in Fig. 2). The graph below shows virtual $\delta^{18}O_c$
 170 (blue) and Δ_{47} (red) records created from these data series using a sampling interval of 0.45 mm and
 171 including analytical noise (see 3.3). Note that the scale of vertical axes varies between plots.

172



173 2.1.3 Virtual cases

174 Virtual SST and $\delta^{18}\text{O}_{\text{sw}}$ time series were constructed to test the effect of various SST and $\delta^{18}\text{O}_{\text{sw}}$ scenarios
175 on the effectivity of the reconstruction methods. The default test case (case 1) contained an ideal, 12-year
176 sinusoidal SST curve with a period of 1 year (seasonality), a mean value of 20°C and a seasonal amplitude
177 of 10°C, a constant $\delta^{18}\text{O}_{\text{sw}}$ value of 0‰VSMOW and a constant growth rate of 10 mm/yr. Other cases
178 contain various deviations from this ideal case (see also **S1**):

- 179 • Linear and/or seasonal changes in growth rate, including growth stops (cases 2-6, 14-18)
- 180 • Seasonal and/or multi-annual changes in $\delta^{18}\text{O}_{\text{sw}}$ (cases 7-11, 13-18)
- 181 • Multi-annual trends in SST superimposed on the seasonality (cases 12, 15 and 17)
- 182 • Variations in the seasonal SST amplitude (cases 19-21)
- 183 • Change in the total length of the time series (cases 22-24).
- 184 • Variation in uncertainty on the age of each virtual datapoint (cases 25-29)

185 Comparison of the virtual time series (case 1-29; **Fig. 2**) with the natural variability (case 30-33; **Fig. 3**)
186 shows that the virtual cases are not realistic approximations of natural variability in SST and $\delta^{18}\text{O}_{\text{sw}}$. Natural
187 SST and $\delta^{18}\text{O}_{\text{sw}}$ variability are not limited to the seasonal or multi-annual scale but contain a fair amount of
188 higher order (daily to weekly scale) variability. In order to simulate this natural variability, we extracted the
189 seasonal component of SST and $\delta^{18}\text{O}_{\text{sw}}$ variability from our highest resolution record of measured natural
190 SST and SSS data (case 30: data from Texel, the Netherlands, see **3.1.2** and **Fig. 3**). The standard
191 deviation of residual variability of this data after subtraction of the seasonal cycle was used to add random
192 high-frequency noise to the SST and $\delta^{18}\text{O}_{\text{sw}}$ variability in virtual cases. Note that while sub-annual
193 environmental variability can be approximated by Gaussian noise (Wilkinson and Ivany, 2002), this
194 representation is an oversimplification of reality. In the case of our Texel data, the SST and SSS residuals
195 are not exactly normally distributed (Kolmogorov-Smirnov test: $D = 0.010$; $p = 7.2 \cdot 10^{-14}$ and $D = 0.039$; $p <$
196 $2.2 \cdot 10^{-16}$ for SST and SSS residuals respectively; see **S2-4**).

197



198 3.2. Subsampling

199 Virtual aliquots were subsampled at equal distance from the SST and $\delta^{18}\text{O}_{\text{sw}}$ depth series of all cases using
200 six sampling intervals: 0.1 mm, 0.2 mm, 0.45 mm, 0.75 mm, 1.55 mm and 3.25 mm. The four largest
201 sampling intervals were chosen such that the standard growth rate (10 mm/yr) was not an integer multiple
202 of the sampling interval (e.g. 0.45 mm instead of 0.5 mm, and 3.25 mm instead of 3 mm). This decision
203 prevents sampling the same parts of the seasonal cycle (e.g. same months) every year, which biases both
204 the mean value and the precision of monthly SST and $\delta^{18}\text{O}_{\text{sw}}$ reconstructions. This bias towards certain
205 parts of the seasonal cycle is much stronger at low sample sizes (large sampling intervals) and is illustrated
206 in **S6**.

207 3.3 Conversion to $\delta^{18}\text{O}_{\text{c}}$ and Δ_{47}

208 After subsampling, SST and $\delta^{18}\text{O}_{\text{sw}}$ were converted to $\delta^{18}\text{O}_{\text{c}}$ and Δ_{47} using a carbonate model based on
209 empirical relationships of Δ_{47} and $\delta^{18}\text{O}_{\text{c}}$ with and SST and $\delta^{18}\text{O}_{\text{sw}}$ (equation 3 and 4; Kim and O'Neil, 1997;
210 Kele et al., 2015; Bernasconi et al., 2018) and the conversion of $\delta^{18}\text{O}$ values from VSMOW to VPDB scale
211 (equation 5; Brand et al., 2014):

$$212 \quad \Delta_{47} = \frac{0.0449 \cdot 10^6}{(\text{SST} + 273.15)^2} + 0.167 \quad (3)$$

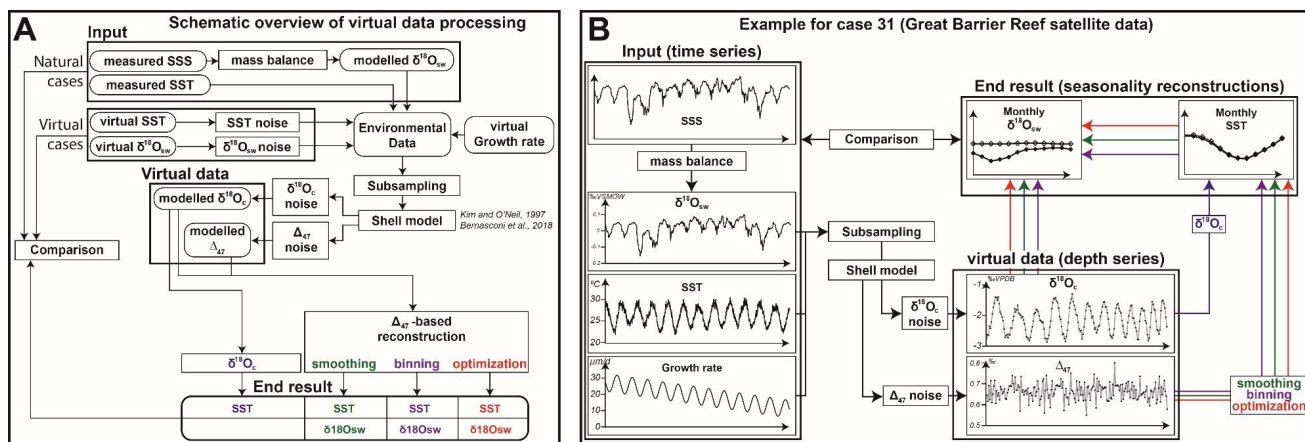
$$213 \quad 1000 * \ln \left(\frac{\left(\frac{^{18}\text{O}}{^{16}\text{O}} \right)_{\text{CaCO}_3}}{\left(\frac{^{18}\text{O}}{^{16}\text{O}} \right)_{\text{H}_2\text{O}}} \right) = 18.03 * \left(\frac{10^3}{(\text{SST} + 273.15)} \right) - 32.42 \quad (4)$$

$$214 \quad \delta^{18}\text{O}_{\text{VPDB}} = 0.97002 * \delta^{18}\text{O}_{\text{VSMOW}} - 29.98 \quad (5)$$

215 The resulting depth records of Δ_{47} and $\delta^{18}\text{O}_{\text{c}}$ and their associated true SST and $\delta^{18}\text{O}_{\text{sw}}$ records are used as
216 basis for comparing the reliability of the approaches in different scenarios. A schematic overview of all steps
217 taken to create virtual data and test the four reconstruction approaches as well as an example of case 30
218 (Great Barrier reef data, see also **Fig. 2**) is provided in **Fig. 4**. All calculations for creating Δ_{47} and $\delta^{18}\text{O}_{\text{c}}$
219 depth series were carried out using the open-source computational software R (R core team, 2013), and
220 scripts for these calculations are given in **S7**. All Δ_{47} and $\delta^{18}\text{O}_{\text{c}}$ datasets are provided in **S8**. In the case of
221 the real oyster data, $\delta^{18}\text{O}_{\text{c}}$ data from Ullmann et al. (2010) was used and Δ_{47} data was created from the



222 seasonal SST record provided in the same study with added natural residual variability (as explained in
223 **3.1.3**).



224

225 **Figure 4:** A) Flow diagram showing the steps taken to create virtual data and compare results of SST and $\delta^{18}O_{sw}$ reconstructions with the actual
 226 SST and $\delta^{18}O_{sw}$ data the record was based on. B) An example of the steps highlighted in A) using case 31 (Great Barrier Reef data) meant to
 227 illustrate the data processing steps. Virtual data plots include normally distributed measurement uncertainty on Δ_{47} and $\delta^{18}O_c$.



228 3.4 SST and $\delta^{18}\text{O}_c$ reconstructions

229 SST and $\delta^{18}\text{O}_{\text{sw}}$ seasonality were reconstructed from the Δ_{47} and $\delta^{18}\text{O}_c$ records to test the reliability of the
230 sample reduction approaches (see **Fig. 1**). In all approaches, a typical analytical uncertainty on
231 measurements of Δ_{47} (one standard deviation of 0.04‰) and $\delta^{18}\text{O}_c$ (one standard deviation of 0.05‰) was
232 used to include measurement precision. These analytical uncertainties were chosen based on typical
233 uncertainties reported for these measurements in the literature (e.g. Schöne et al., 2005; Huyghe et al.,
234 2015; Vansteenberge et al., 2016) and long-term precision uncertainties obtained by measuring in-house
235 standards using the MAT253+ with Kiel IV setup in the clumped isotope laboratory at Utrecht University
236 (e.g. Kocken et al., 2019). Virtual measurement uncertainty was propagated through all reconstruction
237 approaches using a Monte Carlo simulation ($N = 1000$) in which Δ_{47} and $\delta^{18}\text{O}_c$ records were randomly
238 sampled from a normal distribution with the virtual Δ_{47} and $\delta^{18}\text{O}_c$ values as means and analytical
239 uncertainties as standard deviations. For each case study, sampling interval and reconstruction method,
240 SST and $\delta^{18}\text{O}_{\text{sw}}$ results were aggregated into monthly averages, medians, standard deviations, and
241 standard errors. Step by step documentation of calculations made for the three Δ_{47} -based reconstruction
242 approaches and the $\delta^{18}\text{O}_c$ reconstructions are given in **S9** and are detailed below.

243 For $\delta^{18}\text{O}$ reconstructions (**Fig. 1A**), only the $\delta^{18}\text{O}_c$ records were used. Seawater $\delta^{18}\text{O}_{\text{sw}}$ values were
244 assumed to remain 0‰VSMOW throughout the year. The simulated $\delta^{18}\text{O}_c$ records with analytical
245 uncertainties added were directly converted to SST using the Kim and O'Neil (1997) temperature
246 relationship (see equation 4).

247 **Smoothing** reconstructions (**Fig. 1B**) were carried out by defining a range of moving window sizes (from
248 $N=1$ to the complete record). For every simulated Δ_{47} and $\delta^{18}\text{O}_c$ record, all moving windows were tested.
249 The window size that resulted in the most significant difference between maximum and minimum Δ_{47} values
250 using a student's T-test was applied on both Δ_{47} and $\delta^{18}\text{O}_c$ records. This process was repeated for all virtual
251 records to propagate simulated analytical uncertainty through the protocol. SST and $\delta^{18}\text{O}_{\text{sw}}$ were calculated
252 for each set of Δ_{47} and $\delta^{18}\text{O}_c$ records using the combination of empirical temperature relationships by Kim
253 and O'Neil (1997) and Bernasconi et al. (2018; equation 3)



254 In **binning** reconstructions (**Fig. 1C**), virtual Δ_{47} and $\delta^{18}\text{O}_c$ data were grouped into monthly time bins and
255 converted to SST and $\delta^{18}\text{O}_{\text{sw}}$ using the Kim and O'Neil (1997) and Bernasconi et al. (2018) formulae. The
256 prerequisite for this method is that the data is aligned using a (floating) age model accurate enough to allow
257 samples to be placed in the right bin. The age of virtual samples in this study is known so this prerequisite
258 poses no problems in this case, but the same may not be true in the fossil record.

259 Finally, the **optimization** reconstruction approach (**Fig. 1D**) was carried out by ordering the aliquots of each
260 virtual dataset from warm (low $\delta^{18}\text{O}_c$) to cold (high $\delta^{18}\text{O}_c$) data samples, regardless of their position relative
261 to the seasonal cycle. From this ordered dataset, increasingly large samples of multiple aliquots (from $N=1$
262 to the complete record) are taken from both the warm ("summer") and the cold ("winter") side of the
263 distribution. Sample sizes with significant difference in Δ_{47} value between summer and winter groups ($p \leq$
264 0.05 based on a student's T-test) were selected as optimal sample sizes. For each successful sample size,
265 SST and $\delta^{18}\text{O}_{\text{sw}}$ values were calculated from Δ_{47} and $\delta^{18}\text{O}_c$ data according to Kim and O'Neil (1997) and
266 Bernasconi et al. (2018) formulae. The relationship between SST and $\delta^{18}\text{O}_{\text{sw}}$ obtained from these
267 reconstructions was used to convert all data to SST and $\delta^{18}\text{O}_{\text{sw}}$.

268 Accuracy and precision of reconstructions of the following four parameters were evaluated:

- 269 1. mean annual SST (MAT)
- 270 2. seasonal range in SST (temperature difference between warmest and coldest month)
- 271 3. mean annual $\delta^{18}\text{O}_{\text{sw}}$
- 272 4. seasonal range in $\delta^{18}\text{O}_{\text{sw}}$ ($\delta^{18}\text{O}_{\text{sw}}$ difference between warmest and coldest month).

273 Accuracy was defined as the absolute offset of the reconstruction from the actual data. Precision was
274 defined as the (relative) standard deviation of the reconstruction, as calculated from the variability within
275 monthly time bins resulting from error propagation through the reconstruction methods. An overview of
276 monthly SST and $\delta^{18}\text{O}_{\text{sw}}$ reconstructions using the four approaches in all cases is given in **S5**. Raw data
277 results and figures of reconstructions of all cases using all sampling resolutions are compiled in **S10**.

278

279

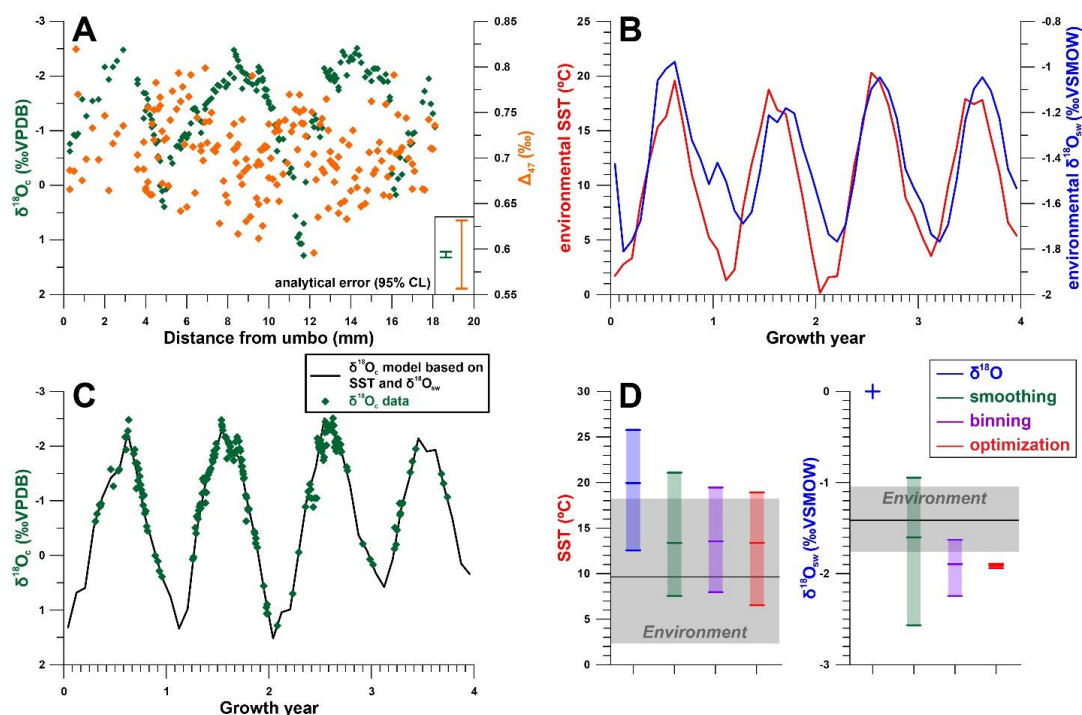


280 **4. Results**

281 **4.1 Real example**

282 Measured ($\delta^{18}\text{O}_c$) and simulated (Δ_{47}) data from the Pacific oyster from the Danish List Basin yield various
283 estimates for SST and $\delta^{18}\text{O}_{\text{sw}}$ seasonality depending on which reconstruction approach is taken (**Fig. 5**).
284 While a model of shell $\delta^{18}\text{O}_c$ based on SST and SSS data closely approximates the measured $\delta^{18}\text{O}_c$ record
285 (**Fig. 5C**), basing SST reconstructions solely on $\delta^{18}\text{O}_c$ data without any *a priori* knowledge of $\delta^{18}\text{O}_{\text{sw}}$
286 variability (assuming constant $\delta^{18}\text{O}_{\text{sw}}$ equal to the global marine value) leads to high inaccuracy in SST
287 seasonality and mean annual SST (**Fig. 5D**). The in-phase relationship between SST and SSS (**Fig. 5B**)
288 dampens the seasonal $\delta^{18}\text{O}_c$ cycle, causing underestimation of temperature seasonality, while a negative
289 mean annual $\delta^{18}\text{O}_{\text{sw}}$ value in the List Basin biases SST reconstructions towards higher temperatures. In
290 terms of SST reconstructions, the **smoothing**, **binning** and **optimization** approaches based on Δ_{47} and
291 $\delta^{18}\text{O}_c$ data yield more accurate reconstructions, albeit with a reduced seasonality and a bias towards the
292 summer season. The latter is a result of severely reduced growth rates in the winter season, which was
293 therefore undersampled (see **Fig. 5A** and **5C**). Approaches including Δ_{47} data also yield far more accurate
294 $\delta^{18}\text{O}_{\text{sw}}$ estimates than the $\delta^{18}\text{O}$ approach. However, the accuracy on both seasonality and mean annual
295 $\delta^{18}\text{O}_{\text{sw}}$ estimates is high in these approaches too, largely because of the limited sampling resolution,
296 especially in winter. The **optimization** approach suffers especially from the strong in-phase relationship
297 between SST and SSS, which obscures the difference between the $\delta^{18}\text{O}_{\text{sw}}$ effect and the temperature effect
298 on shell carbonate. Yet, disentangling SST from $\delta^{18}\text{O}_{\text{sw}}$ seasonality is central to the success of the approach
299 (see **3.4**). **Fig. 5D** does not show the reproducibility error on SST and $\delta^{18}\text{O}_{\text{sw}}$ estimates, which is much
300 larger for the **smoothing** approach than for the **binning** and **optimization** approaches due to the limited
301 data in the winter seasons (see **S5**).

302 These results highlight that several properties of carbonate archives, such as growth rate variability, phase
303 relationships between SST and $\delta^{18}\text{O}_{\text{sw}}$ seasonality and sampling resolution, can negatively impact the
304 reliability of paleoseasonality reconstructions. The virtual and real data cases in this study were tailored to
305 test the effects of these archive properties more thoroughly.



306

307 **Figure 5:** (A) Plot of $\delta^{18}O_c$ and (virtual) Δ_{47} data from a modern Pacific oyster (*Crassostrea gigas*; see
 308 Ullmann et al., 2010). (B) shows SST and $\delta^{18}O_{sw}$ data from the List Basin (Denmark) in which the oyster
 309 grew. (C) shows the fit between $\delta^{18}O_c$ data and modelled $\delta^{18}O_c$ calculated from SST and $\delta^{18}O_{sw}$ on which
 310 the shell age model was based. (D) Shows a summary of the results of different approaches for
 311 reconstructing SST and $\delta^{18}O_{sw}$ from the $\delta^{18}O_c$ and Δ_{47} data. The vertical colored bars show the
 312 reconstructed seasonal variability using all methods with ticks indicating warmest month, coldest month,
 313 and annual mean. The grey horizontal bars show the actual seasonal variability in the environment.
 314 Precision errors on monthly reconstructions are not shown but are given in S5.

315

316 3.2 Case specific results

317 A case-by-case breakdown of the precision (Fig. 6) and accuracy (Fig. 7) of reconstructions using the four
 318 approaches shows that reliability of reconstructions varies significantly between approaches and is highly
 319 case-specific. In general, precision is highest in $\delta^{18}O$ reconstructions, followed by **optimization** and
 320 **binning** with **smoothing** generally yielding the worst precision. Average precision standard deviations of
 321 the underperforming methods (**binning** and **smoothing**) are up to 2-3 times larger than those of $\delta^{18}O$ (e.g.
 322 respectively 3.9°C and 3.5°C vs. 1.3°C for $\delta^{18}O$ MAT reconstructions). It is worth noting that precision on
 323 $\delta^{18}O$ -based estimates is mainly driven by measurement precision (which is better for $\delta^{18}O$ than for Δ_{47}



324 measurements, see section 5.1.1), while Δ_{47} -based reconstructions lose precision due to the higher
325 measurement error on Δ_{47} measurements and the method used for combining measurements for
326 seasonality reconstructions. On a case-by-case basis, the hierarchy of approaches can differ, especially if
327 strong variability in growth rate is introduced, such as in case 14, where the size of hiatuses in the record
328 increases progressively, or in case 18, in which half of the year is missing due to growth hiatuses (see S1
329 and S5). Between the Δ_{47} -based methods (**smoothing**, **binning** and **optimization**), **optimization** is rarely
330 outcompeted in terms of precision in both SST and $\delta^{18}\text{O}_{\text{sw}}$ reconstructions.

331 The comparison based on precision alone is misleading, as the approach which is most precise (**$\delta^{18}\text{O}$**) runs
332 the risk of being highly inaccurate (offsets exceeding 4°C on some MAT reconstructions; see Fig. 7C),
333 especially in cases based on natural SST and SSS (case 30-33). The **smoothing** approach also often
334 yields highly inaccurate results, especially in cases with substantial variability in $\delta^{18}\text{O}_{\text{sw}}$ (e.g. case 9-11).
335 Accuracy of **optimization** and **binning** outcompete the other methods in most circumstances. **Binning**
336 outperforms **optimization** in reconstructions of $\delta^{18}\text{O}_{\text{sw}}$ seasonality, making it overall the most accurate
337 approach. Interestingly, **optimization** is less accurate specifically in cases with sharp changes in growth
338 rate in summer (e.g. cases 11, 14, 16 and 17), with **binning** performing better in these cases.
339 Reconstructions of mean annual SST and $\delta^{18}\text{O}_{\text{sw}}$ of case 18 are especially inaccurate regardless of which
340 method is applied. This extreme case with hiatuses lasting half of the year combined with seasonal
341 fluctuations in both SST and $\delta^{18}\text{O}_{\text{sw}}$ presents a worst-case scenario for seasonality reconstructions leading
342 to strong biases in mean annual temperature reconstructions. In situations like case 18, the **optimization**
343 approach is most accurate in MAT and SST seasonality reconstructions, but $\delta^{18}\text{O}_{\text{sw}}$ is more accurately
344 reconstructed using the **binning** approach. Finally, it is worth noting that in natural situations (Fig. 3),
345 variability in SST almost invariably has a larger influence on $\delta^{18}\text{O}$ and Δ_{47} records, such that fluctuations in
346 $\delta^{18}\text{O}$ records closely follow the SST seasonality even in cases with relatively large $\delta^{18}\text{O}_{\text{sw}}$ variability (e.g.
347 case 30). Chronologies based on these $\delta^{18}\text{O}$ fluctuations are therefore generally accurate.

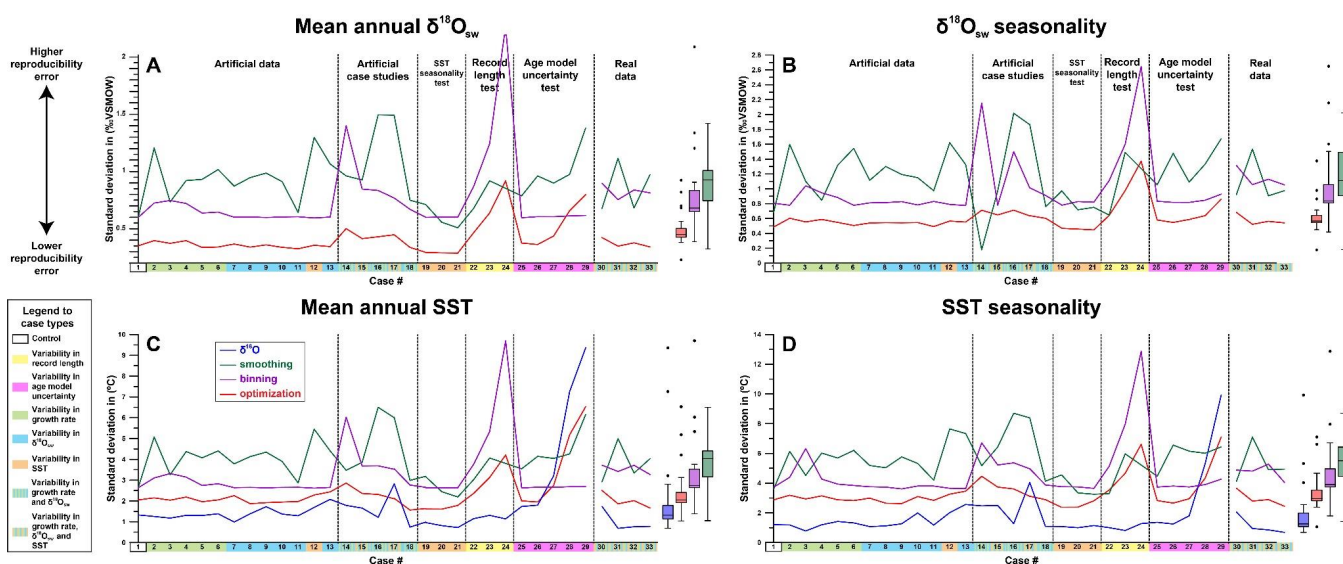


Figure 6: Overview of precision (one standard deviation) of reconstructions of mean annual $\delta^{18}\text{O}_{\text{sw}}$ (A), seasonal range in $\delta^{18}\text{O}_{\text{sw}}$ (B), mean annual SST (C) and seasonal range in SST (D), with higher values indicating lower precision (higher precision errors) based on average sampling resolution (sampling interval of 0.45 mm). The horizontal axis displays the different cases, color coded by their difference from the control case (case 1; see legend on the left-hand side). Colored lines indicate the different data treatment approaches. Box-whisker plots to the right show medians and distributions of precision on cases using different reconstruction approaches (outliers are identified as black dots based on 2x interquartile distance). Color coding follows the scheme in Fig. 1.

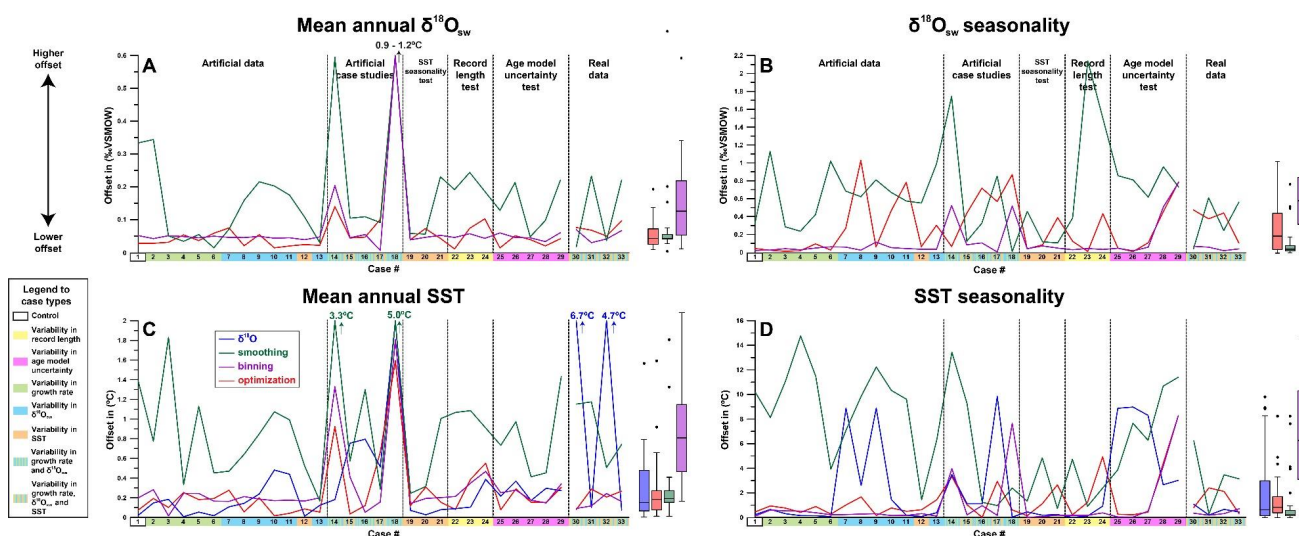
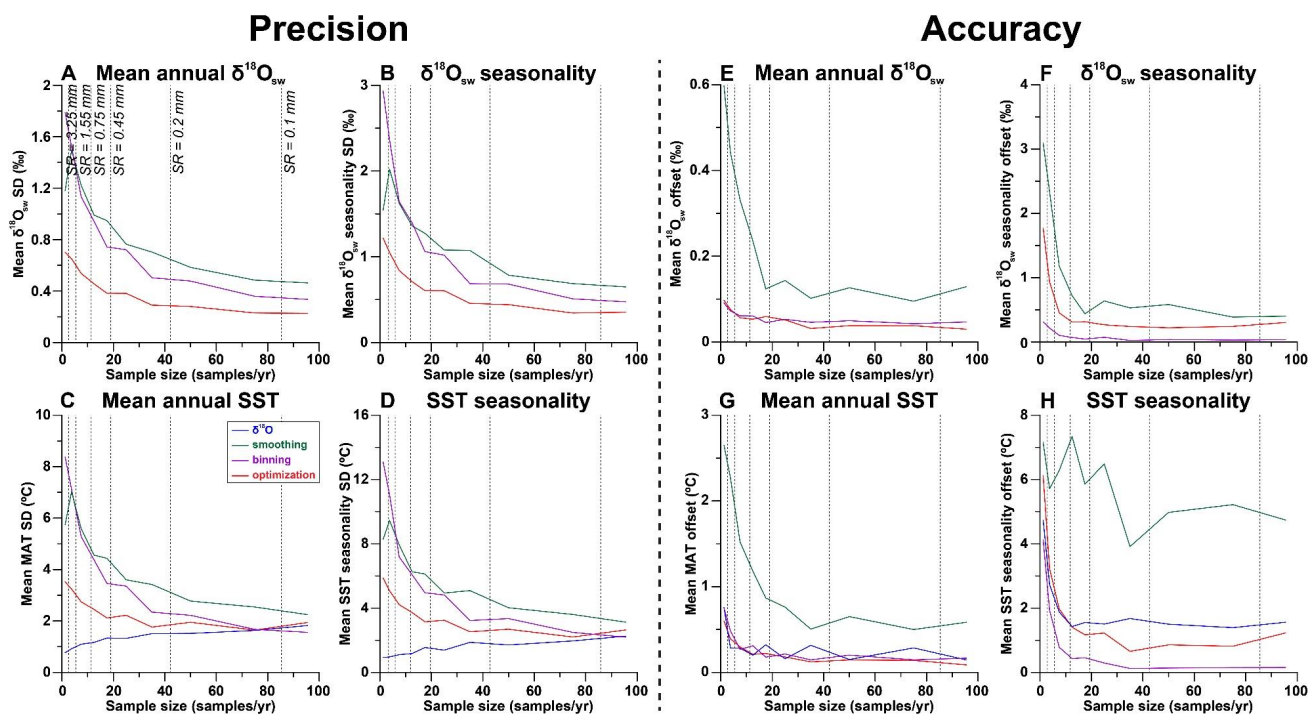


Figure 7: Overview of accuracy (absolute offset from actual values) of reconstructions of mean annual $\delta^{18}\text{O}_{\text{sw}}$ (A), seasonal range in $\delta^{18}\text{O}_{\text{sw}}$ (B), mean annual SST (C) and seasonal range in SST (D), with higher values indicating lower accuracy (higher offsets) based on average sampling resolution (sampling interval of 0.45 mm). The horizontal axis displays the different cases, color coded by their difference from the control case (case 1; see legend on the left-hand side). Box-whisker plots to the right show medians and distributions of accuracy on cases using different reconstruction approaches (outliers are identified as black dots based on 2x interquartile distance). Color coding follows the scheme in Fig. 1 and Fig. 6.



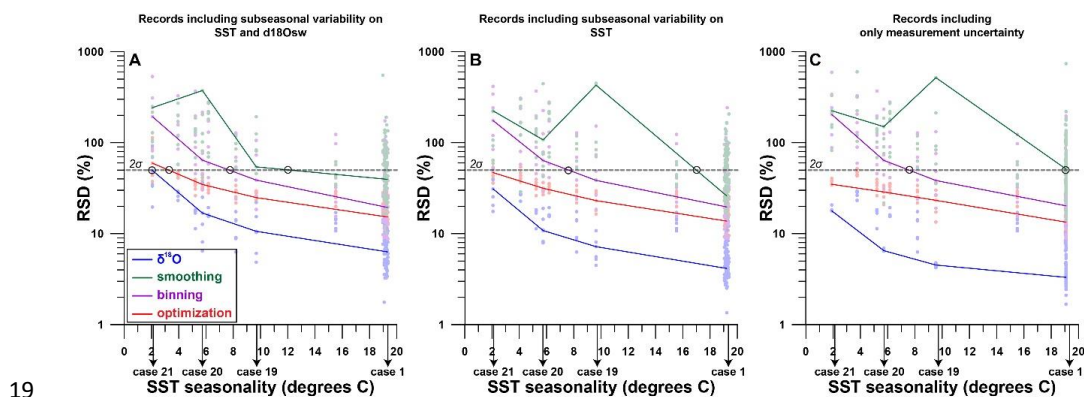
1

2 **Figure 8:** Effect of sampling resolution (in samples per year, see S5) on the precision (one standard deviation) of results of reconstructions of mean
 3 annual $\delta^{18}\text{O}_{\text{sw}}$ (A), seasonal range in $\delta^{18}\text{O}_{\text{sw}}$ (B), mean annual SST (C) and seasonal range in SST (D). Effect on the accuracy (absolute offset from
 4 actual value) of results of reconstructions of mean annual $\delta^{18}\text{O}_{\text{sw}}$ (E) and seasonal range in $\delta^{18}\text{O}_{\text{sw}}$ (F), mean annual SST (G) and seasonal range
 5 in SST (H). Color coding follows the scheme in Fig. 1 and Fig. 4.



6 4.3 Effect of sampling resolution

7 As expected, increasing the temporal sampling resolution (i.e. number of samples per year) almost
8 invariably increases the precision and accuracy (**Fig. 8**) of reconstructions using all methods. An exception
9 to this rule is the precision of $\delta^{18}\text{O}$ reconstructions, which decreases with increasing sampling resolution.
10 Precision errors of all Δ_{47} -based approaches eventually converge with the initially much lower precision
11 error of $\delta^{18}\text{O}$ reconstructions when sampling resolution increases. However, the sampling resolution that is
12 required for Δ_{47} -based reconstructions to rival or outcompete the $\delta^{18}\text{O}$ reconstructions differs, with
13 **optimization** requiring lower sampling resolutions than the other methods (e.g. 20-40 samples/year
14 compared to 40-80 samples year for **smoothing** and **binning**; **Fig. 8A-D**). Accuracy also decreases with
15 sampling resolution (**Fig. 8E-H**). When grouping all cases together, it becomes clear that $\delta^{18}\text{O}$
16 reconstructions can only approach the accuracy of Δ_{47} -based approaches for reconstructions of MAT.
17 Seasonality in both SST and $\delta^{18}\text{O}_{\text{sw}}$ is most accurately reconstructed using **binning**, and the **smoothing**
18 approach once again performs worst.



20 **Figure 9:** Effect of SST seasonality range (difference between warmest and coldest month) in the record
21 on the relative precision of SST seasonality reconstructions (one standard deviation divided by the mean
22 value). Panel **A** shows precision results if random variability (“weather patterns”) in both SST and $\delta^{18}\text{O}_{\text{sw}}$
23 as well as measurement uncertainty is added to the records (see 3.1.1 and **S1**). Panel **B** shows precision
24 of records with random variability in SST and measurement uncertainty only. Panel **C** shows precision if
25 only measurement uncertainty is considered. Color coding follows the scheme in **Fig. 1** and **Fig. 4**. Shaded
26 dots represent results at various sampling resolutions, while bold lines are averages for all reconstruction
27 approaches. Black circles highlight the places where curves cross the threshold of two standard deviations,
28 which indicates the minimum SST seasonality that can be resolved within 2 standard deviations (~95%
29 confidence level) using the reconstruction approach.

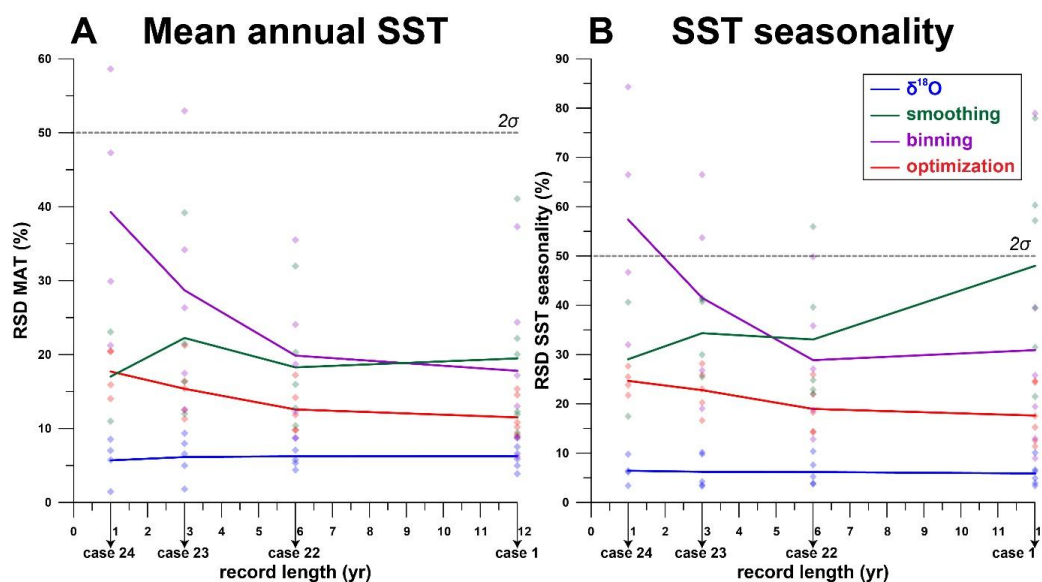
30



31 **4.4 Resolving SST seasonality**

32 Comparison of cases 19, 20 and 21 (SST seasonality of 9.7°C, 5.7°C and 2.1°C respectively) with control
33 case 1 (SST seasonality of 19.3°C) allowed us to study how changes in the seasonal SST range affect the
34 precision of measurements (**Fig. 9**; see also **S1**). The data reconfirms that $\delta^{18}\text{O}$ reconstructions are most
35 precise; a deceptive statistic given the risk of highly inaccurate results this approach yields (see **Fig. 7**).
36 Taking into consideration only analytical uncertainty, all approaches except for **smoothing** can confidently
37 resolve at least the highest SST seasonality within a significance level of two standard deviations (~95%)
38 using a moderate sampling resolution (mean of all resolutions shown in **Fig. 10**). Increasing sampling
39 resolution improves the precision of Δ_{47} -based reconstructions (see **Fig. 8D**), so high sampling resolutions
40 (0.1 or 0.2 mm) allow smaller seasonal differences to be resolved. When random sub-annual variability is
41 added to the SST and $\delta^{18}\text{O}_{\text{sw}}$ records (see 3.1.3 and **S1**), the minimum seasonal SST extent that can be
42 resolved decreases for all approaches (**Fig. 9B** and **9C**). Nevertheless, $\delta^{18}\text{O}$ and **optimization**
43 reconstructions remain able to resolve a relatively small SST seasonality of 2-4°C, even with all noise added
44 to the records.

45



46

47 **Figure 10:** Effect of record length (in years) on the relative precision (one standard deviation as fraction of
 48 the mean value) of results of reconstructions of mean annual SST (A) and SST seasonality (B). Shaded
 49 dots represent results for the six different sampling resolutions. Solid lines connect averages for cases 1,
 50 22, 23 and 24 for each reconstruction approach. Color coding follows the scheme in Fig. 1 and Fig. 4.

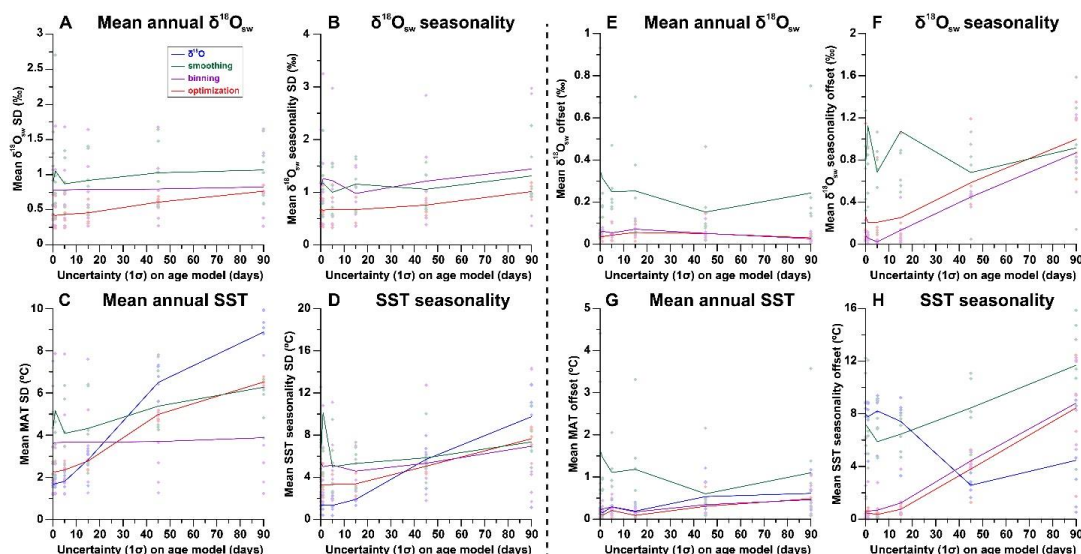
51

52 4.5 Effect of record length

53 The effect of variation in the length of the record was investigated by comparing cases 22, 23 and 24 (record
 54 length of 6 years, 3 years and 1 year) with the control case (record length of 12 years; see Fig. 10 and S1).
 55 As expected, the precision of MAT and SST seasonality results slightly increases in larger datasets (longer
 56 records). However, this pattern is not clear in **smoothing** and $\delta^{18}\text{O}$ reconstructions. The difference between
 57 reconstruction approaches remains relatively constant regardless of the length of the record, with general
 58 precision hierarchy remaining intact ($\delta^{18}\text{O}$ > **optimization** > **binning** > **smoothing**). An exception occurs
 59 in the case of very short records (1-2 years), where the **smoothing** gains an advantage over other Δ_{47} -
 60 based methods due to its lack of sensitivity to changes in the record length. For very short (<3 yr) records,
 61 **binning** reconstructions are not precise enough to resolve MAT and SST seasonality within two standard
 62 deviations (~95% confidence level). Most of the variation in precision with record length is driven by very
 63 high precision errors of reconstructions based on records with low sampling resolutions (sampling intervals



64 of 1.55 mm or 3.25 mm; see also **Fig. 8A-D**). As a result, most of the reduction in precision in shorter
65 records can be mitigated by denser sampling.



66

67 **Figure 11:** Effect of uncertainty in age model on the reproducibility (standard deviation on estimate) of
68 results of reconstructions of mean annual $\delta^{18}\text{O}_{\text{sw}}$ (**A**) and seasonal range in $\delta^{18}\text{O}_{\text{sw}}$ (**B**), mean annual SST
69 (**C**) and seasonal range in SST (**D**). Effect of uncertainty in age model on the accuracy (offset from true
70 value) of results of reconstructions of mean annual $\delta^{18}\text{O}_{\text{sw}}$ (**E**) and seasonal range in $\delta^{18}\text{O}_{\text{sw}}$ (**F**), mean
71 annual SST (**G**) and seasonal range in SST (**H**). Color coding follows the scheme in **Fig. 1** and **Fig. 4**.

72

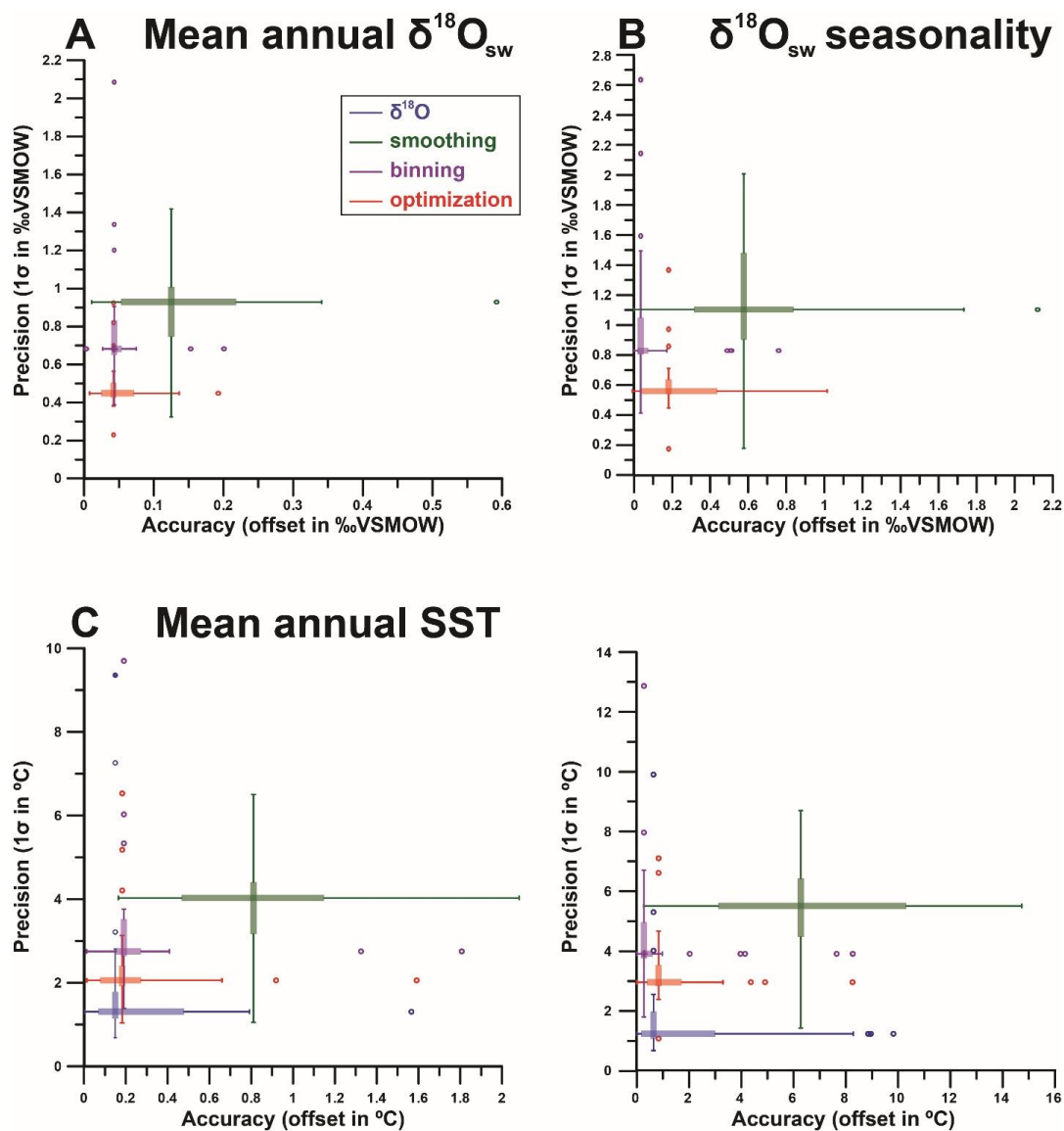
73 4.6 Effect of age model uncertainty

74 Uncertainty on the age model has a significant effect on both the precision and the accuracy (**Fig. 11**) of
75 reconstructions using all approaches. The $\delta^{18}\text{O}$ reconstructions are most strongly affected by uncertainties
76 in the age model and suffer from a large decrease in precision with increasing age model uncertainty (**Fig.**
77 **11C-D**). The high reproducibility of the $\delta^{18}\text{O}$ approach in comparison with the Δ_{47} approaches quickly
78 disappears when age model uncertainty increases beyond 20-30 days. Interestingly, the accuracy of SST
79 seasonality reconstructions based on $\delta^{18}\text{O}$ initially improves with age model uncertainty (**Fig. 11H**).
80 However, this observation is likely caused by the fact that age model uncertainty was compared based on
81 conditions in case 9, which features a phase offset between SST and $\delta^{18}\text{O}_{\text{sw}}$ seasonality causing the $\delta^{18}\text{O}$
82 method to be highly inaccurate even without age model uncertainty. The precision of **smoothing** and



83 **optimization** approaches also decreases with increasing age model uncertainty (**Fig 11A-D**), and the
84 **optimization** approach loses its precision advantage over the **binning** and **smoothing** approaches when
85 age model uncertainty increases beyond 30 days. The monthly **binning** approach is very robust, and its
86 precision does not significantly decrease with increasing age model uncertainty. Seasonality
87 reconstructions through both the **binning** and **optimization** approach quickly lose accuracy when age
88 model uncertainty increases. The accuracy of the **smoothing** approach remains the worst of all approaches
89 in regardless of age model uncertainty (**Fig. 11E-H**).

90



91

92 **Figure 12:** Overview of averages and ranges of accuracy (absolute offset from real value) and precision
93 (one standard deviation from the mean) on mean annual $\delta^{18}\text{O}_{\text{sw}}$ (A) and seasonal range in $\delta^{18}\text{O}_{\text{sw}}$ (B), mean
94 annual SST (C) and seasonal range in SST (D) within all cases using the four different reconstruction
95 approaches. Color coding follows the scheme in Fig. 1 and Fig. 4. Box-whisker plots for precision and
96 accuracy cross at their median values and outliers (colored symbols) are identified based on 2x the
97 interquartile difference (see Fig. 6 and 7)

98



99 **5. Discussion**

100 **5.1 Performance of reconstruction approaches**

101 *5.1.1 $\delta^{18}\text{O}_c$ vs Δ_{47} -based reconstructions*

102 A summary of the general reliability of the four approaches is shown in **Figure 12**. The $\delta^{18}\text{O}$ reconstructions
103 are generally less accurate than Δ_{47} -based reconstructions (especially **binning** and **optimization**; see **Fig**
104 **12** and **S10**). This is a consequence of the assumption that $\delta^{18}\text{O}_{\text{sw}}$ remains constant year-round, and that
105 we know its true value. Both these assumptions are problematic in absence of independent evidence of the
106 value of $\delta^{18}\text{O}_{\text{sw}}$, especially in deep time settings (see e.g. Veizer and Prokoph, 2015; Henkes et al., 2018).
107 The risk of this assumption is made clear when comparing cases in which $\delta^{18}\text{O}_{\text{sw}}$ is indeed constant year-
108 round at the assumed value (0‰VSMOW; e.g. cases 1-6 and 19-24) with cases in which shifts in $\delta^{18}\text{O}_{\text{sw}}$
109 occur, especially when these shifts are out of phase with respect to the SST seasonality (e.g. cases 9-11,
110 18 and 25-33; **Fig. 7C-D**). Cases mimicking or based on natural SST and SSS variability (cases 14-18 and
111 30-33) as well as the modern oyster data (**Fig. 5**) yield stronger inaccuracies in MAT and seasonality
112 reconstructions, showing that even in many modern natural circumstances the assumption of constant
113 $\delta^{18}\text{O}_{\text{sw}}$ is problematic.

114 It is important to consider that the value of mean annual $\delta^{18}\text{O}_{\text{sw}}$ remained very close to the assumed value
115 of 0‰VSMOW (within 0.15‰) in all cases except for natural data cases 30 (-1.55‰VSMOW), 32
116 (1.01‰VSMOW; see **S5**) and the real oyster data (-1.42‰VSMOW; **Fig. 5**). The SST values of these cases
117 reconstructed using $\delta^{18}\text{O}_c$ data show large offsets from their actual values (+6.7°C, -4.7°C and +10.3°C for
118 case 30, case 32 and the real oyster data respectively; see **Fig. 5 and 7C** and **S5**). These offsets are
119 equivalent the temperature offset one might expect from inaccurately estimating $\delta^{18}\text{O}_{\text{sw}}$ (~-4.6
120 °C/‰VSMOW; Kim and O'Neil, 1997) and are only rivaled by the offset in reconstructions of case 18
121 (+5.0°C), which has growth hiatuses obscuring the coldest half of the seasonal cycle. The fact that such
122 differences in $\delta^{18}\text{O}_{\text{sw}}$ exist even in modern environments should not come as a surprise, given the available
123 data on variability of $\delta^{18}\text{O}_{\text{sw}}$ (at least -3‰ to +2‰VSMOW; e.g. LeGrande and Schmidt, 2006) and SSS (30
124 to 40 ; ESA, 2020) in modern ocean basins. However, it should warrant caution in using $\delta^{18}\text{O}_c$ data for SST
125 reconstructions in modern settings. Implications for deep time reconstructions are even greater, given the



126 uncertainty on and variability in global average (let alone local) $\delta^{18}\text{O}_{\text{sw}}$ values (Jaffrés et al., 2007; Veizer
127 and Prokoph, 2015). The complications of using $\delta^{18}\text{O}_{\text{c}}$ as a proxy for marine temperatures in deep time are
128 discussed in detail in O'Brien et al. (2017), and Tagliavento et al. (2019).

129 The analytical uncertainty of individual $\delta^{18}\text{O}_{\text{c}}$ aliquots (typically 1 S.D. of 0.05‰; e.g. de Winter et al., 2018)
130 represents only ~1.1% of the variability in $\delta^{18}\text{O}_{\text{c}}$ over the seasonal cycle (~4.3‰ for the default 20°C
131 seasonality in case 1, following Kim and O'Neil, 1997). This is much smaller than the analytical uncertainty
132 of Δ_{47} (typically 1 S.D. of 0.02-0.04‰; e.g. Fernandez et al., 2018; de Winter et al., 2020), which equates
133 to 25-50% of the seasonal variability in Δ_{47} (~0.08‰ for 20°C seasonality, following Bernasconi et al., 2018;
134 see **S8**). This roughly 20-fold difference in relative precision causes $\delta^{18}\text{O}_{\text{c}}$ based SST reconstructions to be
135 much more precise (see **Figs 6, 8-11**) than those based on Δ_{47} , and forces the necessity for grouping Δ_{47}
136 data in reconstructions. However, as discussed above, the low precision of $\delta^{18}\text{O}$ reconstructions is
137 misleading and not a useful statistic if they are highly inaccurate.

138 Our results show that paleoseasonality reconstructions based on $\delta^{18}\text{O}_{\text{c}}$ can only be relied upon if there is
139 strong independent evidence of the value of $\delta^{18}\text{O}_{\text{sw}}$ and if significant sub-annual variability in $\delta^{18}\text{O}_{\text{sw}}$ (>0.3‰,
140 equivalent to a 2-3°C SST variability; see **Fig. 8-9**; Kim and O'Neil, 1997) can be neglected with confidence.
141 Examples of such cases include fully marine environments unaffected by influxes of (isotopically light)
142 freshwater or evaporation (increasing $\delta^{18}\text{O}_{\text{sw}}$; Rohling, 2013). Carbonate records from suitable
143 environments include, for example, the *A. islandica* bivalves from considerable depth (30-50m) in the open
144 marine Northern Atlantic (e.g. Schöne et al., 2005, on which case 33 is based). Previous reconstruction
145 studies show that $\delta^{18}\text{O}_{\text{sw}}$ in smaller basins such as the Western Interior Seaway are heavily influenced by
146 the processes affecting $\delta^{18}\text{O}_{\text{sw}}$ on smaller scales (e.g. Petersen et al., 2016). Consequently, accurate
147 quantitative reconstructions of seasonal range in shallow marine environments with extreme seasonality
148 may not be feasible using the $\delta^{18}\text{O}$ approach, because these environments are invariably characterized by
149 significant fluctuations in $\delta^{18}\text{O}_{\text{sw}}$ and growth rate.

150 While variability in $\delta^{18}\text{O}_{\text{sw}}$ compromises accurate $\delta^{18}\text{O}$ -based seasonality reconstructions, the compilation
151 in **Fig. 3** shows that its influence on the $\delta^{18}\text{O}$ records is too small to affect the shape of the record to such
152 a degree that seasonality is fully obscured. While natural situations with $\delta^{18}\text{O}_{\text{sw}}$ fluctuations large enough



153 to totally counterbalance the effect of temperature seasonality on $\delta^{18}\text{O}$ records are imaginable, these cases
154 are likely rare. This means that chronologies based on $\delta^{18}\text{O}$ seasonality, which are a useful tool to anchor
155 seasonal variability in absence of independent growth markers (e.g. Judd et al., 2018), are reliable in most
156 natural cases.

157 5.1.2 Seasonality reconstructions using moving averages (*smoothing*)

158 Of the three methods for combining Δ_{47} data, the **smoothing** approach clearly performs worst in all four
159 reconstructed parameters (MAT, SST seasonality, mean annual $\delta^{18}\text{O}_{\text{sw}}$ and $\delta^{18}\text{O}_{\text{sw}}$ seasonality), both in
160 terms of accuracy and precision (**Fig. 12**). While applying a moving average may be a good strategy for
161 lowering the uncertainty of Δ_{47} -based temperature reconstructions in a long time series (e.g. Rodríguez-
162 Sanz et al., 2017), the method underperforms in cases where baseline and amplitude of a periodic
163 component, spike or event (e.g. MAT and SST seasonality) are extracted from a record. This is likely due
164 to the smoothing effect of the moving average, which reduces the seasonal cycle and causes highly
165 inaccurate seasonality reconstructions (offsets mounting to $>6^\circ\text{C}$; **Fig. 12**). This bias is especially
166 detrimental in cases where the seasonal cycle is obscured by seasonal growth halts (e.g. case 18), multi-
167 annual trends in growth (e.g. case 4, 14 and 17) and multi-annual trends in SST (e.g. case 15 and 17; see
168 **Fig. 6** and **Fig. 7**). The lack of performance of the **smoothing** approach can be slightly mitigated by
169 increasing sampling resolution (**Fig 8**), but even at high sampling resolutions (every 0.1 or 0.2 mm) the
170 method still fails to reliably resolve seasonal SST ranges below 5°C even in idealized cases (case 19-21;
171 **Fig. 9**). Increasing the number of samples by analyzing longer records does not improve the result, because
172 smoothing of the seasonal cycle by a moving average window introduces the same dampening bias as long
173 as the temporal sampling resolution (number of samples per year) remains equal (**Fig. 10**).

174 More critically, employing the **smoothing** method may give the illusion that seasonality is more reduced,
175 and severely bias reconstructions. This bias highlights the importance of using the official meteorological
176 definition of seasonality as the difference between the averages of warmest and coldest month in
177 paleoseasonality work (O'Donnell et al., 2012). This definition is much more robust than the “annual range”
178 often cited based on maxima and minima in $\delta^{18}\text{O}_{\text{c}}$ records. This “annual range” strongly depends on
179 sampling resolution, which is typically $<12 \text{ yr}^{-1}$ (Goodwin et al., 2003), equivalent to the third lowest sampling



180 interval (0.75 mm) simulated in this study. Therefore, we strongly recommend future studies to adhere to
181 the monthly definition of seasonality to foster comparison between studies. While inter-annual variability is
182 lost by combining data from multiple years into estimates of WMMT and CMMT, this approach increases
183 precision, accuracy and comparability of paleoseasonality results. Inter-annual variability can still be
184 discussed from plots of raw data against age or depth.

185 *5.1.3 Monthly binning, sample size optimization and age model uncertainty*

186 Overall, the most reliable paleoseasonality reconstructions can be obtained from either **binning** or
187 **optimization** (Fig. 12). In general, **optimization** is slightly more precise, while **binning** yields more
188 accurate estimates of seasonal range in SST and $\delta^{18}\text{O}_{\text{sw}}$ (Fig. 12B and D). The more flexible combination
189 of aliquots in the **optimization** routine yields improved precision (especially on mean annual averages) in
190 cases where parts of the record are undersampled or affected by hiatuses and simultaneous fluctuations
191 in both SST and $\delta^{18}\text{O}_{\text{sw}}$ (e.g. case 3-6, 14---18, 30-33). The downside of this flexibility is that in case of
192 larger sample sizes, the seasonal variability may be dampened, like in the **smoothing** approach (see 5.1.1).
193 The rigid grouping of data in monthly bins in **binning** prevents this dampening and therefore yields slightly
194 more accurate estimates of seasonal ranges in SST and $\delta^{18}\text{O}_{\text{sw}}$. A caveat of **binning** is that it requires a
195 very reliable age model of the record, as least on a monthly scale. If the age model has a large uncertainty,
196 there is a risk that samples are grouped in the wrong month, which compromises the accuracy of **binning**
197 reconstructions, especially for reconstructions of seasonal range (Fig 11H).

198 Techniques for establishing independent age models for climate archives range from counting of growth
199 layers or increments (Schöne et al., 2008; Huyghe et al., 2019), modelling and extracting of rhythmic
200 variability in climate proxies through statistical approaches (e.g. De Ridder et al., 2007; Goodwin et al.,
201 2009; Judd et al., 2018) and interpolation of uncertainty on absolute dates (e.g. Scholz and Hoffman, 2011;
202 Meyers, 2019; Sinnesael et al., 2019). While propagating uncertainty in the data on which age models are
203 based onto the age model is relatively straightforward, errors on underlying *a priori* assumptions such as
204 linear growth rate between dated intervals, (quasi-)sinusoidal forcing of climate cycles and the uncertainty
205 on human-generated data such as layer counting are very difficult to quantify (e.g. Comboul et al., 2014).
206 The uncertainty of such age models of climate records is thus difficult to assess and may not be normally



207 distributed. A simplified test of the effect of a normally distributed error on the age value of each proxy data
208 point (case 25-29) shows that uncertainties in the age domain can significantly compromise reconstructions
209 (**Fig. 11**). Within the scope of this study, only the effect of symmetrical, normally distributed uncertainties
210 on an artificial case with phase decoupled SST and $\delta^{18}\text{O}_{\text{sw}}$ seasonality (case 9) was tested. The effect of
211 other types of uncertainties on other cases remains unknown, highlighting an unknown uncertainty in
212 paleoseasonality and other high-resolution paleoclimate studies that may introduce bias or lead to over-
213 optimistic errors on reconstructions. Future research could aim to quantify this unknown uncertainty by
214 propagating estimates of various types of uncertainty on depth values of samples and on the conversion of
215 depth to time in age models.

216 **5.2 Conditions influencing success of reconstructions**

217 Our results show that the reliability (accuracy and precision) of SST and $\delta^{18}\text{O}_{\text{sw}}$ reconstructions depends
218 on case-specific conditions. The range of cases tested in this study allowed us to evaluate the effect of
219 variability in SST, growth rate, $\delta^{18}\text{O}_{\text{sw}}$, sampling resolution and record length relative to the control case
220 (case 1; see **S1**). A summary of the effects of these changes is given in **Table 1**.

221



Variable	cases	Metric	Effect on reconstructions			
			$\delta^{18}\text{O}$	smoothing	binning	optimization
SST	12	Precision	0	+++	+	0
	15					
	17					
	19-21 30-33	Accuracy	+	+	0	+
Growth rate	2-6	Precision	+	++	++	+
	14-18					
	30-33	Accuracy	+	++	0	+
$\delta^{18}\text{O}_{\text{sw}}$	7-11	Precision	+	++	0	0
	13-18					
	30-33	Accuracy	+++	+++	+	++
Sampling resolution	1-33	Precision	0	+++	++	++
		Accuracy	+	+	+++	+
Record length	22-24	Precision	0	0	+++	++
		Accuracy	+	0	++	++
Age model uncertainty?	25-29	Precision	+++	++	0	++
		Accuracy	+	+	++	++

222 **Table 1:** Qualitative summary of the effects of changes in variables relative from the ideal case on
 223 reconstructions using the four approaches. The “cases” column lists cases in which the changes in the
 224 respective variable relative to the control case (case 1) were represented (see **S1**). “0” = negligible effect,
 225 “+” = weak increase in uncertainty, “++” = moderate increase in uncertainty, “+++” = strong increase in
 226 uncertainty. Details on the precision and accuracy of all tests is given in **S12**.

227

228 5.2.1 SST variability

229 Variability in water temperature most directly affects the proxies under study. By default (case 1), SST is
 230 taken to vary sinusoidally around a MAT of 20°C with an amplitude of 10°C (see 3.1.1, **Fig. 2** and **S1**). In
 231 case of exceptions, in which multi-annual variability in SST is simulated (e.g. case 15 and 17), the accuracy
 232 of SST reconstructions using $\delta^{18}\text{O}$ and **optimization** are reduced, while the **binning** approach is less
 233 strongly affected. Examples of such multi-annual cyclicity are El-Niño Southern Oscillation (ENSO;
 234 Philander, 1983) or North Atlantic Oscillation (NOA; Hurrell, 1995). The effect is especially large in case 17,
 235 which simulates a tropical environment with reduced SST seasonality and a strong multi-annual cyclicity.
 236 This type of environment is analogous to the environment of tropical shallow water corals, which are often
 237 used as archives for ENSO variability (e.g. Charles et al., 1997; Fairbanks et al., 1997). As such, these
 238 virtual records should be analogous to tropical cases from the Australian Great Barrier Reef (case 31) and
 239 Red Sea (case 32; see **Fig. 6-7**). We therefore recommend future researchers to use the **binning** approach



240 on carbonate records where multi-annual cyclicity is prevalent and if a reliable age model can be
241 established for these records (as in e.g. Sato, 1999; Scourse et al., 2006; Miyaji et al., 2010).

242 5.2.2 Growth rate variability and hiatuses

243 **Figures 6 and 7** show that variations in the growth rate of records, including the occurrence of hiatuses,
244 have a strong effect on reconstructions, especially using the **smoothing** approach. In general, hiatuses
245 and slower growth reduce precision of monthly SST and $\delta^{18}\text{O}_{\text{sw}}$ reconstructions by reducing mean temporal
246 sampling resolution (samples/yr; see **Fig. 8**), and because specific parts of the record are undersampled.
247 The effect on accuracy depends strongly on the timing of changes in growth rate or the occurrence of
248 hiatuses. Cases 26 simulate specific growth rate effects and can be used to test these differences. The
249 **smoothing** method is especially sensitive to changes in growth rate that take place in specific seasons,
250 such as hiatuses in winter (case 2) or summer (case 3) and growth peaks in summer (case 5) or spring
251 (case 6). The other reconstruction approaches are less affected by this bias, because they generally do not
252 mix samples from different seasons and therefore produce less smoothing. The $\delta^{18}\text{O}$ method is especially
253 well suited to deal with changes in growth rate because it does not require combining different aliquots for
254 accurate SST reconstructions. The **binning** and **optimization** approaches are slightly less accurate in
255 cases where growth rate decreases linearly or seasonally along the entire record (cases 46; **Fig. 5**). This
256 likely occurs because these two methods consider all samples in the records at once, instead of only a
257 subset at any one time (as in the **smoothing** method), and are therefore more sensitive to changes in
258 temporal sampling resolution along the record. It is worth noting that **optimization** is especially sensitive to
259 sharp changes in growth rate in summer (e.g. cases 11, 14, 16 and 17) because those conditions force the
260 **optimization** routine to use larger sample sizes or include samples outside the warmest month for summer
261 temperature estimates.

262 A worst-case scenario of reconstructions hampered by growth rate variability and hiatuses is represented
263 by case 18, where the entire cold half of the year is not recorded. Such cases result in strong biases in
264 reconstructions of mean annual and seasonal ranges in SST and $\delta^{18}\text{O}_{\text{sw}}$, regardless of which method is
265 used. In such extreme cases the record simply contains insufficient information to reconstruct variability in
266 growth rate, SST and $\delta^{18}\text{O}_{\text{sw}}$, and it seems that no statistical method would enable this missing information



267 to be recovered. In such cases, the only way to eliminate bias in reconstructions would be to establish
268 reliable age models, independent of $\delta^{18}\text{O}$ or Δ_{47} data, which show that a large part of the seasonal cycle is
269 missing.

270 While hiatuses encompassing half of the seasonal cycle are uncommon, changes in growth rate are
271 common in accretionary carbonate archives because conditions for (biotic or abiotic) carbonate
272 mineralization often vary over time. This variability is either driven by biological constraints, such as
273 senescence (e.g. Schöne, 2008; Hendriks et al., 2012), reproductive cycle (Gaspar et al., 1999) or stress
274 (Surge et al., 2001; Compton et al., 2007) or by variations in the environment that promote or inhibit
275 carbonate production, such as seasonal variations temperature (Crossland, 1984; Bahr et al., 2017) or
276 precipitation (Dayem et al., 2010; Van Rampelbergh et al., 2014). In general, such conditions occur more
277 frequently in mid- to high-latitude environments than in low-latitudes, and in more coastal environments
278 rather than in open marine settings, because these environments contain stronger variations in the factors
279 that influence growth rates (e.g. temperature, precipitation or freshwater influx; e.g. Surge et al., 2001;
280 Ullmann et al., 2010). This difference was simulated the cases representing natural variability (case 14-18
281 and 30-33), with accuracy in the coastal high-latitude settings (cases 16, 18 and 29) more strongly affected
282 by changes in growth rate. Because in such highly variable environments growth rate variability often co-
283 occurs with variability in $\delta^{18}\text{O}_{\text{sw}}$, using $\delta^{18}\text{O}_{\text{c}}$ -based reconstructions is not advised, unless $\delta^{18}\text{O}_{\text{sw}}$ variability
284 can be constrained or neglected (which is rare in these environments). An additional complication is that
285 growth rate variability cannot always be resolved because of uncertainties in the record's age model (see
286 **4.1.3**). Therefore, reconstructions in these highly dynamic environments may not allow all variables that
287 introduce bias to be isolated, and irregular variability in growth rate and $\delta^{18}\text{O}_{\text{sw}}$ will invariably introduce
288 uncertainty in SST reconstructions, even when applying the best Δ_{47} -based approaches (e.g. **binning** and
289 **optimization**). In such examples, the results of natural variability cases (14-18 and 30-33) and of the real
290 oyster data (**Fig. 5**) may serve as benchmarks for the degree of uncertainty that may remain unexplained
291 in these records.

292



293 *5.2.3 Variability in $\delta^{18}\text{O}_{\text{sw}}$*

294 Large increases in uncertainty on reconstructions are caused by variations in $\delta^{18}\text{O}_{\text{sw}}$ (see **Fig. 6 and 7**). As
295 discussed in **4.1.1**, these variations have a large effect on the accuracy of $\delta^{18}\text{O}_{\text{c}}$ -based reconstructions,
296 and their occurrence constitutes the main advantage of applying the Δ_{47} thermometer (Eiler, 2011).
297 However, results of cases 7-11 in **Fig. 7** and **Table 1** show that $\delta^{18}\text{O}_{\text{sw}}$ variations can also bias Δ_{47} -based
298 reconstructions, especially those of seasonal ranges and using the **smoothing** approach. **Smoothing**
299 reconstructions are biased by these $\delta^{18}\text{O}_{\text{sw}}$ shifts in much the same way as they are affected by shifts in
300 growth rate (see **4.1.2**). The **optimization** approach, especially when used for reconstructions of $\delta^{18}\text{O}_{\text{sw}}$
301 seasonality, is sensitive to seasonal changes in $\delta^{18}\text{O}_{\text{sw}}$ in antiphase with SST seasonality and by increases
302 in $\delta^{18}\text{O}_{\text{sw}}$ in summer (e.g. due to excess evaporation). This effect arises because the **optimization**
303 approach orders data based on $\delta^{18}\text{O}_{\text{c}}$ and Δ_{47} seasonality to isolate the $\delta^{18}\text{O}_{\text{sw}}$ -SST relationship. Both
304 antiphase $\delta^{18}\text{O}_{\text{sw}}$ seasonality and summer evaporation dampens the seasonal $\delta^{18}\text{O}_{\text{c}}$ cycle and therefore
305 influences the reconstruction of the $\delta^{18}\text{O}_{\text{sw}}$ -SST relationship. A good example of this is seen in the real
306 oyster data (**Fig. 5**), where $\delta^{18}\text{O}_{\text{sw}}$ and SST vary in phase and $\delta^{18}\text{O}_{\text{sw}}$ dampens the SST seasonality. The
307 **binning** approach is more robust against $\delta^{18}\text{O}_{\text{sw}}$ variability that dampens the seasonal cycle and is therefore
308 a better choice for absolute SST reconstructions in environments where summer evaporation or other
309 $\delta^{18}\text{O}_{\text{sw}}$ variability in phase with SST seasonality is expected to occur, if the age model is reliable enough to
310 allow monthly binning of raw data (see **4.1.3**). Indeed, reconstructions from the lagoonal environment (case
311 16) and Red Sea case (case 32 which is characterized by strong summer evaporation; e.g. Titschack et
312 al., 2010) show that **binning** is the most reliable choice in these environments.

313 *5.2.4 Variability in sampling resolution and record length*

314 Other factors influencing the effectivity of reconstructions are the sampling resolution and the length of the
315 record. Many of the cases discussed in this study represent idealized cases with comparatively high
316 sampling resolutions over comparatively long (12 yr) paleoseasonality records, which yield large sample
317 sizes. By comparison, the typical age of mollusks, which are often used as paleoseasonality archives, is 2-
318 5 years (Ivany, 2012). Records with the highest sampling resolutions (0.1 and 0.2 mm) contain up to 1200
319 samples. This is not an unfeasible number of samples, but it is highly unlikely to be applied in paleoclimate



320 studies given the limitation of resources (e.g. instrument time) and the desire to analyze multiple records
321 from different specimens, species, localities or ages to gain a better understanding of the variability in
322 paleoseasonality (e.g. Goodwin et al., 2003; Schöne et al., 2006; Petersen et al., 2016). In some cases
323 large datasets are meticulously collected from single carbonate records (e.g. Schöne et al., 2005;
324 Vansteenberge et al., 2016; de Winter et al., 2020a; Shao et al., 2020). However, in such studies, the aim
325 is often to investigate variability at a higher (e.g. daily; de Winter et al., 2020a) resolution or longer
326 timescales (e.g. decadal to millennial; Schöne et al., 2005; Vansteenberge et al., 2016; Shao et al., 2020)
327 in addition to the seasonal cycle, rather than to improve the reliability of reconstructing one type of variability
328 (e.g. seasonality) alone. In this study, extreme (sometimes unnatural, e.g. case 18) cases were chosen
329 deliberately to explore the effect of different conditions and guide researchers in deciding their sampling
330 strategy to optimize their samples and resources in function to their various research goals.

331 **Fig. 8** shows that increasing temporal sampling resolution (samples/yr) improves both the accuracy and
332 precision of all Δ_{47} -based reconstructions. This occurs because Δ_{47} samples have a large analytical
333 uncertainty (see 5.1.2) and grouping of data therefore improves reconstructions. Interestingly, in $\delta^{18}\text{O}_c$ -
334 based reconstructions precision decreases with increasing sample size while accuracy increases (**Fig. 8C-**
335 **D**). This is explained by the fact that the analytical uncertainty of $\delta^{18}\text{O}_c$ measurements is much smaller than
336 the variability introduced by natural sub-annual variability in SST and $\delta^{18}\text{O}_{\text{sw}}$ unrelated to the seasonal cycle
337 (see S4). Therefore, higher sampling resolutions allow $\delta^{18}\text{O}_c$ records to better capture this sub-seasonal
338 variability, which introduces more noise on the seasonal cycle (reducing precision) but causes monthly
339 mean SST and $\delta^{18}\text{O}_{\text{sw}}$ to be more accurately reconstructed. Towards higher sampling resolutions, the gap
340 in precision between $\delta^{18}\text{O}_c$ - and Δ_{47} -based reconstructions closes, eventually (in an ideal case) diminishing
341 the advantage of high analytical precision in $\delta^{18}\text{O}_c$ measurements (**Fig. 8C-D**).

342 The rate of increase in precision and accuracy with sampling resolution is not the same for each method,
343 and an optimum sample resolution can be defined for each method after which improving sampling
344 resolution does not significantly improve the reliability of the reconstruction (as in de Winter et al., 2017).
345 **Figure 8** shows that this optimum is different depending on which variable (MAT, SST seasonality, mean
346 annual $\delta^{18}\text{O}_{\text{sw}}$ or $\delta^{18}\text{O}_{\text{sw}}$ seasonality) is reconstructed. Therefore, **Fig. 8** will allow future researchers to



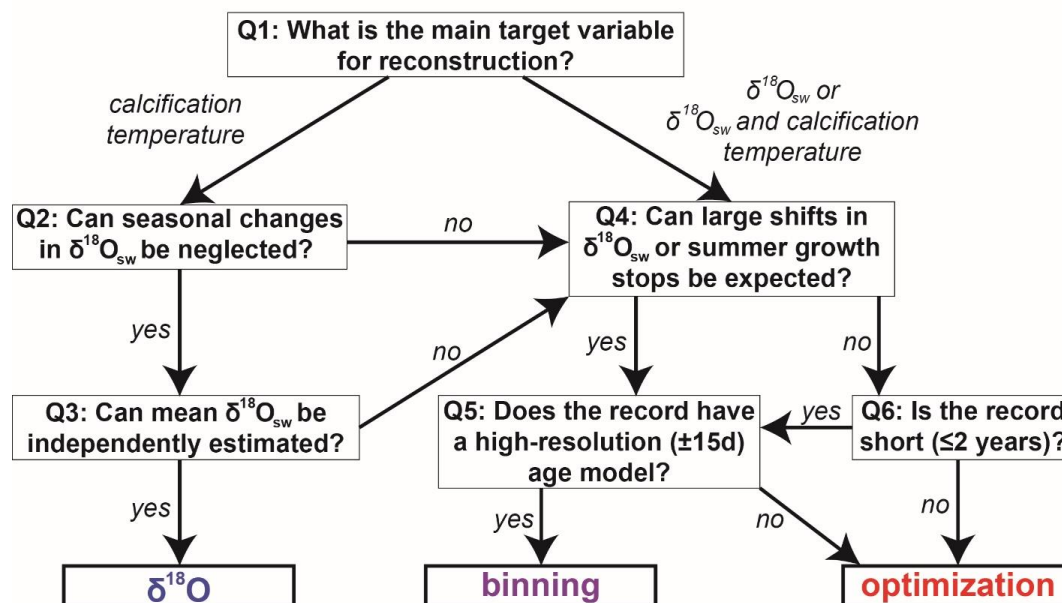
347 determine the sampling resolution that is tailored to their purpose. In general, the improvement after a
348 sample size of 20-30 samples per year is negligible for the **binning** and **optimization** methods if the total
349 number of samples (depending on both sampling resolution and record length) is sufficient for monthly
350 temperature reconstructions. Our data show that 200-250 paired $\delta^{18}\text{O}_c$ and Δ_{47} measurements are in
351 general sufficient for a standard deviation of 2-3°C on monthly SST reconstructions using the **binning** or
352 **optimization** approach (**Fig. 8; S5**).

353 Record length only has a minimal influence on the **optimization** method but for very short records (≤ 2
354 years) **binning** becomes very imprecise, especially at low sampling resolutions (**Fig. 10**). The reason for
355 this is that the sample size within monthly time bins becomes too small in these cases, while the more
356 flexible sample size window of the optimization routine circumvents this problem. The choice between these
357 two approaches should therefore be based on a tradeoff between the length of the record (in time) and the
358 number of samples that can be retrieved from it. As a result, shorter-lived, fast-growing climate archives,
359 such as large or fast-growing (e.g. juvenile) mollusk shells, are best sampled using a high temporal
360 resolution (30+ samples/yr) sampling strategy with the **optimization** approach. Longer lived archives with
361 a lower mineralization rate, such as annually laminated speleothems, corals and gerontic mollusks, are
362 best sampled using long time series at monthly resolution using the **binning** approach.

363 A simplified decision tree that could guide sampling strategies for future paleoseasonality studies is shown
364 in **Figure 13**. Note that choices and tradeoffs for these reconstructions may differ depending on the archive
365 and environment in which it formed (see discussion above).



Schematic guide to reconstructing SST and $\delta^{18}\text{O}_{\text{sw}}$ from accretionary carbonate archives



366

367 **Figure 15:** Schematic guide to choosing the right approach for reconstructing annual mean or seasonality
368 in SST and $\delta^{18}\text{O}_{\text{sw}}$ from accretionary carbonate archives. Recommendations are based on the results of
369 testing all four approaches on the entire range of cases. Researchers can follow the six steps (questions
370 Q1-6) to decide on the right approach for reconstructing the target variable. Guidelines are based on
371 minimizing both accuracy and precision (see details in S11). Note that the **smoothing** approach is never
372 the best choice. The choice between the two remaining Δ_{47} -based approaches (**binning** and **optimization**)
373 relies heavily on the situation and may be driven by a preference for more accurate or more precise results.

374

375 5.3 Implications for clumped isotope sample size

376 The **optimization** technique for grouping Δ_{47} aliquots for accurate SST and $\delta^{18}\text{O}_{\text{sw}}$ reconstructions allows
377 us to assess the limitations of the clumped isotope thermometer for temperature reconstructions from high-
378 resolution carbonate archives. The actual optimal sample size given by the approach is different for different
379 cases and depends on the temporal sampling resolution and the characteristics of the record (see S5). As
380 expected, in cases more similar to the ideal case (case 1), optimal sample sizes are low (~14--24), while
381 sample sizes quickly increase in more complicated cases based on simulated natural environments (case
382 14--18) or cases based on actual SST and SSS data (cases 30-33). More confined SST seasonality (cases
383 19-21) also requires larger samples to reconstruct (up to 100 samples in some cases). This is not surprising,



384 because variability within samples will increase in more complicated records in which the seasonality is
385 smaller or more obscured by other environmental variability. The optimal sample size between cases and
386 sampling resolutions is not normally distributed but tails towards high sample sizes with some extreme
387 outliers (Shapiro Wilk test $p \ll 0.05$; **S12**). The median sample size of all our simulations is 17 aliquots.
388 This number lies between the minimum number of 14 ~100 μg replicates of standards calculated by
389 Fernandez et al. (2017) and the minimum of 20-40 ~100 μg aliquots required for optimal paleoseasonality
390 reconstruction from fossil bivalves by de Winter et al. (2020a). This is to be expected since many of the
391 cases explored in this study represent ideal cases compared with the natural situation. However, in many
392 cases a measure of random sub-annual variability in SST and $\delta^{18}\text{O}_{\text{sw}}$ was added (see **S2**), simulating a
393 more realistic environment and resulting in poorer precision than replicates of a carbonate standard (as in
394 Fernandez et al., 2017). Our simulations show that the optimum number of samples to be combined in
395 seasonality studies depends on both the analytical uncertainty of Δ_{47} measurements (as represented by
396 the estimate in Fernandez et al., 2017) and the variability between aliquots pooled within a sample that is
397 attributed to actual variability within the record (as represented by our simulations and the estimate in de
398 Winter et al. 2020a). The optimal sample size is therefore a good measure for the limitations of temperature
399 variability that can be resolved in a record. As such, this number, together with the overview in **S1**, can help
400 researchers decide which strategy to apply for combining measurements to obtain the most reliable
401 paleoseasonality estimates, or to decide whether extra sampling is required, even if the chosen approach
402 is not to use the **optimization** routine itself.

403 **5.4 Implications for other sample size problems**

404 While the discussion above focuses on optimizing approaches for combining samples for clumped isotope
405 analyses in paleoseasonality reconstructions, the problem of combining samples to lower uncertainty and
406 isolate variation in datasets is very common (e.g. Zhang et al., 2004; Merz and Thieken, 2005; Tsukakoshi,
407 2011). Therefore, the approaches outlined and tested in this study have applications beyond
408 paleoseasonality reconstructions. Below, we briefly highlight four examples of problems that could benefit
409 from applying similar approaches for lowering the uncertainty of estimates of target variables or reducing
410 the number of analyses required to meet analytical requirements.



411 *5.4.1 Tooth bioapatite*

412 Enamel from vertebrate teeth constitute a useful archive for paleoenvironmental and paleoecological
413 change in the terrestrial realm, complementing the carbonate records discussed in this work (e.g. Luz and
414 Kolodny, 1985; Fricke et al., 1996; Balasse, 2002; Van Dam and Reichart, 2009; de Winter et al., 2016).
415 However, the tooth bioapatite archive suffers from similar limitations of sample size and resolution as
416 carbonate archives when it comes to reconstructing high-resolution variability (see discussion in Passey
417 and Cerling, 2002 and Kohn, 2004). Oxygen and carbon isotopes of carbonate and phosphate in tooth
418 enamel contain valuable information about the animal's life cycle and environment (e.g. Fricke et al., 1996;
419 Balasse et al., 2002; Van Dam and Reichart, 2009). However, structurally bound carbonate constitutes a
420 mere 2-5% of tooth enamel (LeGeros et al., 1986), and enamel samples need to be pretreated to remove
421 labile components, so analyses of $\delta^{18}\text{O}$ in these archives require comparatively large sample sizes (0.5-1
422 mg; Fricke et al., 1998; Balasse, 2002; Pellegrini and Snoeck, 2016). Phosphate-bound $\delta^{18}\text{O}$ is less
423 susceptible to diagenesis, but requires a more complicated procedure to analyze, resulting in similar sample
424 size limitations (Joachimski et al., 2002; Lecuyer et al., 2007). Most applications of isotope profiles from
425 teeth rely on precise determination of both the phase and amplitude of the seasonal cycle, and therefore
426 suffer from the same complications as isotope records in carbonate archives (e.g. Balasse et al., 2002;
427 Straight et al., 2004). The **binning** and **optimization** approaches discussed here could help reduce
428 uncertainty and provide a basis for better comparison of seasonal profiles in tooth enamel.

429 *5.4.2 Cyclostratigraphy*

430 Within the field of cyclostratigraphy, a multitude of stratigraphical approaches have been developed for
431 signal processing, with the aim to use regular orbital cycles expressed in stratigraphic time series as tools
432 for dating rock sequences (e.g. Paillard et al., 1996; Meyers, 2014; Sinnesael et al., 2016). However, the
433 focus on timing has caused many methods for extracting the climatic impact of these orbital cycles from
434 stratigraphic records (e.g. bandpass filtering; Hilgen, 1991) to remain qualitative. This is unfortunate,
435 because the magnitude of the effect of this cyclicity on climate and environmental change is of major interest
436 in paleoclimatology studies (e.g. Berger, 1992; Shackleton, 2000; Zachos et al., 2001; Lourens et al., 2005;
437 De Vleeschouwer et al., 2017a). The problem of quantitatively extracting the impact of orbital cycles is very



438 similar to the problem of paleoseasonality reconstructions central to this study, and the same approaches
439 can therefore be used in the orbital time domain. The time **binning** approach is probably most robust for
440 this purpose, since cyclostratigraphic records are often longer (record length \gg period of the cycle) and
441 sampling resolutions (samples/cycle) are often lower than in seasonal records (see **5.2.4**; e.g. De
442 Vleeschouwer et al., 2017b). Quantitative analyses of the contribution of orbital cyclicity to rhythmic
443 changes in paleoclimate can help separate variability in records caused by external forcing from autocyclic
444 behavior or (positive or negative) feedback of the climate system itself (Lourens et al., 2010; Noorbergen
445 et al., 2017; Nohl et al., 2018).

446 *5.4.3 Strontium isotope dating*

447 Another type of analysis that could benefit from smart combination of measurement results is strontium
448 isotope dating. The strontium isotope composition ($^{87}\text{Sr}/^{86}\text{Sr}$) of the ocean has evolved over time, and the
449 isotopic composition of marine carbonates can therefore be used to estimate the age of the sample by
450 comparing it with a composite strontium isotope curve (Elderfield, 1986; McArthur et al., 2012). In time
451 intervals where the global marine strontium isotope curve is steep, strontium isotope dating ranks among
452 the most precise methods for absolute dating in stratigraphy (Wegreich et al., 2012). However, accurate
453 dating based on the strontium isotope curve requires propagation of errors on the composite curve and the
454 sample. Doing so results in asymmetric errors due to the non-linear character of the strontium isotope
455 curve, which require complex error propagation (see Barlow, 2003; 2004; Wan et al., 2019). The state-of-
456 the-art uncertainty of individual strontium isotope analyses ranges between 210 ppm (1 standard deviation;
457 Yobregat et al., 2017), which translates to an age uncertainty of 100-200 kyr, (1 standard deviation)
458 depending strongly on the slope of the global strontium isotope curve at the time interval under study.
459 Combining multiple strontium isotope analyses from the same stratigraphic unit can reduce the uncertainty
460 on these composite ages (Korte and Ullmann, 2016; de Winter et al., 2020b), allowing the dating method
461 to be combined with cyclostratigraphy to produce for orbital scale age models (see **5.4.2**). In stratigraphy
462 studies that use this dating method, the need arises to compromise between the resolution of the age model
463 and the precision and accuracy of dating, analogous to the tradeoff that occurs when combining Δ_{47}
464 analyses for paleoseasonality reconstructions outlined in this study. In this case, the **smoothing** approach



465 with a dynamic moving window discussed in this study is likely the best candidate for combining data to
466 improve these age models. Such an approach can be seen as a more flexible adaptation of the Δ_{47} -based
467 approach for SST reconstruction outlined in Rodríguez-Sanz et al. (2017) that provides the flexibility to
468 adapt the sample window depending on the available data and the slope of the global strontium curve. At
469 the same time, the shape of the global composite strontium isotope curve itself can be refined by using a
470 similar protocol on well-dated samples. The approaches discussed in this study are more adaptable to
471 changes in sampling density over time and can in theory achieve higher precision than the LOWESS fit
472 approach currently employed for constructing the global composite (McArthur et al., 2012). Similarly,
473 techniques for compromising between sampling resolution and accuracy and precision can be applied to
474 improve other dating methods based on matching curves such as radiocarbon dating (Ramsay and Lee,
475 2013), carbon isotope stratigraphy (Salzman and Thomas, 2012) and dendrochronology (Cook and
476 Kairiukstis, 2013).

477 *5.4.4 Sub-seasonal variability*

478 Ultra-high-resolution records from fast-growing archives (e.g. mollusks) are an emerging phenomenon in
479 the field of high-resolution paleoclimatology (e.g. Sano et al., 2012; Warter and Müller, 2017, de Winter et
480 al., 2020a). The emergence of such records allows new information to be obtained about the daily cycle
481 (Warter et al., 2018; de Winter et al., 2020a) and extreme weather events (Yan et al., 2020) in the past,
482 potentially bridging the gap between weather and climate reconstructions. The sampling resolution required
483 to resolve variability at such a fine temporal scale warrants an even more careful consideration of the
484 tradeoff between sample size, sampling resolution and analytical uncertainty than the paleoseasonality
485 examples considered here. If quantitative estimates of insolation, temperature and the frequency of extreme
486 weather events are to be reconstructed from these novel records, a compromise will need to be found
487 between analytical uncertainty and the temporal resolution of measurements (Sano et al., 2012; de Winter
488 et al., 2020a; Yan et al., 2020). Applying the temporal (e.g. hourly) binning method (**binning**) discussed
489 here on long, (sub-)daily resolved records could yield more accurate and precise records of ultra-high-
490 resolution variability, given its reliability in extracting accurate cycle amplitude (e.g. seasonality) from long,
491 less densely sampled records (see 5.1.3). Fast-growing bivalve and gastropod shells have already been



492 marked as promising archives for such variability, while other fast-growing archives such as *Acropora* corals
493 remain to be explored (Bak et al., 2009; Strauss et al., 2014; de Winter et al., 2020c). It must be noted that
494 models for the timing of carbonate deposition in accretionary carbonate archives at the sub-daily scale are
495 highly uncertain and that this may complicate the use of the **binning** approach (see **5.1.3**), in which case
496 **optimization** may be more appropriate.

497 *5.4.5 Event stratigraphy*

498 Accurate and precise temperature reconstructions of short-lived (10-100 kyr) episodes of climate change
499 present a problem comparable to resolving seasonality in paleoclimate archives. Examples of such events
500 include the Mesozoic ocean anoxic events (Hesselbo et al., 2000; Jenkyns, 2010), early Paleogene
501 hyperthermals (Stap et al., 2010; Lauretano et al., 2015, 2018) and stepwise climate perturbations such as
502 the Eocene-Oligocene transition (Dupont-Nivet et al., 2007; Lear et al., 2008) studied in deep-sea records.
503 Currently, reconstructions of temperature variability in the deep-sea during such events are based on
504 benthic foraminiferal $\delta^{18}\text{O}_c$ (e.g. Erbacher et al., 2001; Lui et al., 2009; Stap et al., 2010; Lauretano et al.,
505 2015, 2018), but may not be reliable due to assumptions made on $\delta^{18}\text{O}_{sw}$. Deep-sea sedimentary
506 environments are generally characterized by low sedimentation rates (~ 1 cm/kyr) as well as low abundance
507 and small size of microfossils (e.g. foraminifera) which serve as archives of past marine conditions (e.g.
508 Stap et al., 2010; Jennions et al., 2015). This limits the number of aliquots that can be obtained for Δ_{47} and
509 other analyses through these climate events. In these studies, a **smoothing** approach would probably
510 underestimate the 'true' amplitude of temperature or geochemical change. With sufficient record length and
511 perhaps by combining multiple events, **binning** or **optimization** based on proxy data would be the most
512 accurate and precise approach to resolve transient temperature change in the deep-sea during the
513 geological past.

514



515 6. Conclusions and recommendations

516 The reliability of three Δ_{47} -based approaches to reconstruct seasonality from accretionary carbonate
517 archives was evaluated in comparison with the conventional $\delta^{18}\text{O}_c$ -based reconstructions in a wide range
518 of case studies. From the results, we conclude that while $\delta^{18}\text{O}_c$ -based reconstructions (**$\delta^{18}\text{O}$**) yield superior
519 precision for SST reconstructions, this method runs a high risk of yielding inaccurate results due to innate
520 assumptions about the value of $\delta^{18}\text{O}_{\text{sw}}$, which has to be estimated and assumed constant year-round.
521 Unless a $\delta^{18}\text{O}_{\text{sw}}$ can be independently constrained or variability in $\delta^{18}\text{O}_{\text{sw}}$ can be neglected, Δ_{47} -based
522 reconstructions should be the method of choice for absolute mean annual temperature and SST seasonality
523 reconstructions. Various techniques for combining Δ_{47} data were evaluated. Our findings suggest that
524 smoothing Δ_{47} data using a moving average (**smoothing**) results in almost all cases in a dampening of the
525 seasonal cycle which severely hampers recovery of seasonality. Applying the **smoothing** approach results
526 in inaccuracies in reconstructions of MAT as well, especially in cases where part of the seasonal cycle is
527 obscured by variability in growth rate or multi-annual trends. More reliable seasonality reconstructions are
528 achieved with two approaches for combining Δ_{47} data using time binning (**binning**) or applying a flexible
529 sample size optimization (**optimization**) approach. Of these two approaches, **optimization** achieves better
530 precision and can resolve smaller seasonal temperature differences with confidence. However, **binning** is
531 often more accurate, and outperforms **optimization** as the most reliable approach. This is especially true
532 in cases with growth stops or $\delta^{18}\text{O}_{\text{sw}}$ changes in phase with temperature seasonality (e.g. strong seasonal
533 evaporation or freshwater influx) and in longer multi-annual time series with a reliable age model.
534 **Optimization** is the better choice for shorter (<3 years) records, especially if the sampling resolution can
535 be increased, such as in short, fast growing climate archives.

536 Despite the distinct focus on the problem of resolving seasonality in carbonate archives, the findings in this
537 study have applications for other problems where sample size and sampling resolution put limits on the
538 ability to resolve specific trends, events and cycles from time series. Examples include, but are not limited
539 to, resolving sub-annual variability in geochemical records from tooth bioapatite, quantifying the impact of
540 orbital cycles on paleoclimate, refining strontium isotope dating by strategic sample combination, resolving
541 daily scale variability and weather patterns in ultra-high-resolution climate records and quantifying the



542 impact of climate events in the geological record. While the above mentioned recommendations of the
543 **optimization** and **binning** methods are likely valid for most studies aiming to quantify the mean and
544 amplitude of a specific cycle or event (equivalent to MAT and SST seasonality), (dynamic) moving averages
545 (**smoothing**) are expected to yield the best results in studies quantifying aperiodic trends from longer data
546 series.

547

548 **Code availability**

549 Annotated R scripts used to make calculations for this study are available in the digital supplement uploaded
550 to the open-source online repository Zenodo (www.doi.org/10.5281/zenodo.3899926).

551

552 **Data availability**

553 Supplementary data, figures and tables as well as all scripts used to do the calculations and create the
554 virtual datasets used in this study are deposited in the open-source online repository Zenodo
555 (www.doi.org/10.5281/zenodo.3899926).

556

557 **Author contributions**

558 NJW designed the study, wrote the scripts for all calculations, and created a first draft of the manuscript
559 text and figures. MZ, TA and NJW worked together from the first draft towards the final manuscript. All
560 authors contributed to the representation of the data and methods in figures and to the discussion of the
561 implications of the data in the discussion.

562

563 **Competing Interests**

564 The authors have no potential conflicts of interest to declare with regards to this study.

565



566 Acknowledgements

567 The authors would like to thank all members of the Clumped Isotope research group of Utrecht University,
568 most notably Ilja Kocken and dr. Inigo Müller, for their comments and recommendations on a presentation
569 of the initial results of this study.

570

571 Financial support

572 NJW is funded by the European Commission through a Marie Skłodowska Curie Individual Fellowship
573 (UNBIAS, grant # 843011) and by the Flemish Research Council (FWO) through a Junior Postdoctoral
574 Fellowship (12ZB220N).

575

576 References

- 577 Bahr K. D., Jokiel P. L. and Rodgers K. S. (2017) Seasonal and annual calcification rates of the Hawaiian reef coral, *Montipora capitata*, under
578 present and future climate change scenarios. *ICES J Mar Sci* **74**, 1083–1091.
- 579 Bak R. P., Nieuwland G. and Meesters E. H. (2009) Coral growth rates revisited after 31 years: what is causing lower extension rates in *Acropora*
580 *palmata*? *Bulletin of Marine Science* **84**, 287–294.
- 581 Balasse M. (2002) Reconstructing dietary and environmental history from enamel isotopic analysis: time resolution of intra-tooth sequential
582 sampling. *International Journal of Osteoarchaeology* **12**, 155–165.
- 583 Balasse M., Ambrose S. H., Smith A. B. and Price T. D. (2002) The Seasonal Mobility Model for Prehistoric Herders in the South-western Cape
584 of South Africa Assessed by Isotopic Analysis of Sheep Tooth Enamel. *Journal of Archaeological Science* **29**, 917–932.
- 585 Barlow R. (2004) Asymmetric errors. *arXiv preprint physics/0401042*.
- 586 Barlow R. (2003) Asymmetric systematic errors. *arXiv preprint physics/0306138*.
- 587 Berger A. L. (1992) Astronomical theory of paleoclimates and the last glacial-interglacial cycle. *Quaternary Science Reviews* **11**, 571–581.
- 588 Bernasconi S. M., Müller I. A., Bergmann K. D., Breitenbach S. F., Fernandez A., Hodell D. A., Jaggi M., Meckler A. N., Millan I. and Ziegler M.
589 (2018) Reducing uncertainties in carbonate clumped isotope analysis through consistent carbonate-based standardization. *Geochemistry,*
590 *Geophysics, Geosystems* **19**, 2895–2914.
- 591 Bowen, G.J. (2020) WaterIsotopes.org. Available at: <http://wateriso.utah.edu/waterisotopes> Accessed August 4, 2020.
- 592 Brand W. A., Coplen T. B., Vogl J., Rosner M. and Prohaska T. (2014) Assessment of international reference materials for isotope-ratio analysis
593 (IUPAC Technical Report). *Pure and Applied Chemistry* **86**, 425–467.
- 594 Briard J., Pucéat E., Vennin E., Daëron M., Chavagnac V., Jaillet R., Merle D. and de Rafélis M. (2020) Seawater paleotemperature and paleosalinity
595 evolution in neritic environments of the Mediterranean margin: Insights from isotope analysis of bivalve shells. *Palaeogeography,*
596 *Palaeoclimatology, Palaeoecology* **543**, 109582.
- 597 Charles C. D., Hunter D. E. and Fairbanks R. G. (1997) Interaction between the ENSO and the Asian monsoon in a coral record of tropical climate.
598 *Science* **277**, 925–928.
- 599 Comboul M., Emile-Geay J., Evans M. N., Mirmateghi N., Cobb K. M. and Thompson D. M. (2014) A probabilistic model of chronological errors
600 in layer-counted climate proxies: applications to annually banded coral archives. *Climate of the Past* **10**, 825–841.
- 601 Compton T. J., Rijkkenberg M. J. A., Drent J. and Piersma T. (2007) Thermal tolerance ranges and climate variability: A comparison between
602 bivalves from differing climates. *Journal of Experimental Marine Biology and Ecology* **352**, 200–211.
- 603 Cook E. R. and Kairiukstis L. A. (2013) *Methods of dendrochronology: applications in the environmental sciences.*, Springer Science & Business
604 Media.
- 605 Cramer B. S., Toggweiler J. R., Wright J. D., Katz M. E. and Miller K. G. (2009) Ocean overturning since the Late Cretaceous: Inferences from a
606 new benthic foraminiferal isotope compilation. *Paleoceanography* **24**. Available at:
607 <http://agupubs.onlinelibrary.wiley.com/doi/abs/10.1029/2008PA001683> [Accessed March 31, 2020].
- 608 Crossland C. (1984) Seasonal variations in the rates of calcification and productivity in the coral *Acropora formosa* on a high-latitude reef. *Marine*
609 *Ecology Progress Series* **15**, 135–140.
- 610 van Dam J. A. and Reichart G. J. (2009) Oxygen and carbon isotope signatures in late Neogene horse teeth from Spain and application as temperature
611 and seasonality proxies. *Palaeogeography, Palaeoclimatology, Palaeoecology* **274**, 64–81.
- 612 Dattalo P. (2008) *Determining Sample Size: Balancing Power, Precision, and Practicality.*, Oxford University Press, USA.



- Dayem K. E., Molnar P., Battisti D. S. and Roe G. H. (2010) Lessons learned from oxygen isotopes in modern precipitation applied to interpretation of speleothem records of paleoclimate from eastern Asia. *Earth and Planetary Science Letters* **295**, 219–230.
- De Ridder F., de Brauwere A., Pintelon R., Schoukens J., Dehairs F., Baeyens W. and Wilkinson B. H. (2007) Comment on: Paleoclimatic inference from stable isotope profiles of accretionary biogenic hardparts—a quantitative approach to the evaluation of incomplete data, by Wilkinson, B.H., Ivany, L.C., 2002. *Palaeogeogr. Palaeoclimatol. Palaeoecol.* **185**, 95–114. *Palaeogeography, Palaeoclimatology, Palaeoecology* **248**, 473–476.
- De Vleeschouwer D., Da Silva A.-C., Sinnesael M., Chen D., Day J. E., Whalen M. T., Guo Z. and Claeys P. (2017a) Timing and pacing of the Late Devonian mass extinction event regulated by eccentricity and obliquity. *Nature Communications* **8**, 1–11.
- De Vleeschouwer D., Vahlenkamp M., Crucifix M. and Pälike H. (2017b) Alternating Southern and Northern Hemisphere climate response to astronomical forcing during the past 35 my. *Geology* **45**, 375–378.
- de Winter N., Sinnesael M., Makarona C., Vansteenberge S. and Claeys P. (2017) Trace element analyses of carbonates using portable and micro-X-ray fluorescence: Performance and optimization of measurement parameters and strategies. *Journal of Analytical Atomic Spectrometry* **32**, 1211–1223.
- de Winter N. J., Goderis S., Malderen S. J. M. V., Sinnesael M., Vansteenberge S., Snoeck C., Belza J., Vanhaecke F. and Claeys P. (2020a) Subdaily-Scale Chemical Variability in a Torretites Sanchezi Rudist Shell: Implications for Rudist Paleobiology and the Cretaceous Day-Night Cycle. *Paleoceanography and Paleoclimatology* **35**, e2019PA003723.
- de Winter N. J., Snoeck C. and Claeys P. (2016) Seasonal Cyclicity in Trace Elements and Stable Isotopes of Modern Horse Enamel. *PLoS one* **11**, e0166678.
- de Winter N. J., Ullmann C. V., Sørensen A. M., Thibault N., Goderis S., Van Malderen S. J. M., Snoeck C., Goolaerts S., Vanhaecke F. and Claeys P. (2020b) Shell chemistry of the boreal Campanian bivalve *Rastellum diluvianum*; (Linnaeus, 1767) reveals temperature seasonality, growth rates and life cycle of an extinct Cretaceous oyster. *Biogeosciences* **17**, 2897–2922.
- de Winter N. J., Vellekoop J., Clark A. J., Stassen P., Speijer R. P. and Claeys P. (2020c) The giant marine gastropod *Campanile giganteum* (Lamarck, 1804) as a high-resolution archive of seasonality in the Eocene greenhouse world. *Geochemistry, Geophysics, Geosystems* **11a**, e2019GC008794.
- de Winter N. J., Vellekoop J., Vorsellmans R., Golreihani A., Soete J., Petersen S. V., Meyer K. W., Casadio S., Speijer R. P. and Claeys P. (2018) An assessment of latest Cretaceous Pycnodonte vesicularis (Lamarck, 1806) shells as records for palaeoseasonality: a multi-proxy investigation. *Climate of the Past* **14**, 725–749.
- Denton G. H., Alley R. B., Comer G. C. and Broecker W. S. (2005) The role of seasonality in abrupt climate change. *Quaternary Science Reviews* **24**, 1159–1182.
- Dupont-Nivet G., Krijgsman W., Langereis C. G., Abels H. A., Dai S. and Fang X. (2007) Tibetan plateau aridification linked to global cooling at the Eocene–Oligocene transition. *Nature* **445**, 635–638.
- Elderfield H. (1986) Strontium isotope stratigraphy. *Palaeogeography, palaeoclimatology, palaeoecology* **57**, 71–90.
- Erbacher J., Huber B. T., Norris R. D. and Markey M. (2001) Increased thermohaline stratification as a possible cause for an ocean anoxic event in the Cretaceous period. *Nature* **409**, 325–327.
- Fairbanks R. G., Evans M. N., Rubenstone J. L., Mortlock R. A., Broad K., Moore M. D. and Charles C. D. (1997) Evaluating climate indices and their geochemical proxies measured in corals. *Coral Reefs* **16**, S93–S100.
- Fernandez A., Müller I. A., Rodríguez-Sanz L., van Dijk J., Looser N. and Bernasconi S. M. (2017) A reassessment of the precision of carbonate clumped isotope measurements: implications for calibrations and paleoclimate reconstructions. *Geochemistry, Geophysics, Geosystems* **18**, 4375–4386.
- Fricke H. C. and D’Neil J. R. (1996) Inter- and intra-tooth variation in the oxygen isotope composition of mammalian tooth enamel phosphate: implications for. *Palaeogeography, Palaeoclimatology, Palaeoecology* **126**, 91–99.
- Gaspar M. B., Ferreira R. and Monteiro C. C. (1999) Growth and reproductive cycle of *Donax trunculus* L., (Mollusca: Bivalvia) off Faro, southern Portugal. *Fisheries Research* **41**, 309–316.
- Goodwin D. H., Paul P. and Wissink C. L. (2009) MoGroFunGen: A numerical model for reconstructing intra-annual growth rates of bivalve molluscs. *Palaeogeography, Palaeoclimatology, Palaeoecology* **276**, 47–55.
- Goodwin D. H., Schöne B. R. and Dettman D. L. (2003) Resolution and fidelity of oxygen isotopes as paleotemperature proxies in bivalve mollusk shells: models and observations. *Palaios* **18**, 110–125.
- Harwood A. J. P., Dennis P. F., Marca A. D., Pilling G. M. and Millner R. S. (2008) The oxygen isotope composition of water masses within the North Sea. *Estuarine, Coastal and Shelf Science* **78**, 353–359.
- Hendriks I. E., Basso L., Deudero S., Cabanellas-Reboredo M. and Álvarez E. (2012) Relative growth rates of the noble pen shell *Pinna nobilis* throughout ontogeny around the Balearic Islands (Western Mediterranean, Spain). *Journal of Shellfish Research* **31**, 749–756.
- Henkes, G. A., Passey, B. H., Grossman, E. L., Shenton, B. J., Yancey, T. E. and Pérez-Huerta, A. (2018) Temperature evolution and the oxygen isotope composition of Phanerozoic oceans from carbonate clumped isotope thermometry. *Earth and Planetary Science Letters* **490**, 40–50, doi:10.1016/j.epsl.2018.02.001.
- Hesselbo S. P., Gröcke D. R., Jenkyns H. C., Bjerrum C. J., Farrimond P., Morgans Bell H. S. and Green O. R. (2000) Massive dissociation of gas hydrate during a Jurassic oceanic anoxic event. *Nature* **406**, 392–395.
- Hilgen F. J. (1991) Astronomical calibration of Gauss to Matuyama sapropels in the Mediterranean and implication for the Geomagnetic Polarity Time Scale. *Earth and Planetary Science Letters* **104**, 226–244.
- Hurrell J. W. (1995) Decadal trends in the North Atlantic Oscillation: regional temperatures and precipitation. *Science* **269**, 676–679.
- Huybers P. and Curry W. (2006) Links between annual, Milankovitch and continuum temperature variability. *Nature* **441**, 329.
- Huyghe D., Lartaud F., Emmanuel L., Merle D. and Renard M. (2015) Palaeogene climate evolution in the Paris Basin from oxygen stable isotope ($\delta^{18}O$) compositions of marine molluscs. *Journal of the Geological Society* **172**, 576–587.
- Huyghe D., de Rafélis M., Ropert M., Mouchi V., Emmanuel L., Renard M. and Lartaud F. (2019) New insights into oyster high-resolution hinge growth patterns. *Marine biology* **166**, 48.
- IPCC (2013) *IPCC, 2013: Climate Change 2013: The Physical Science Basis. Contribution of Working Group I to the Fifth Assessment Report of the Intergovernmental Panel on Climate Change*, 1535 pp., Cambridge Univ. Press, Cambridge, UK, and New York.
- Ivany L. C. (2012) Reconstructing paleoseasonality from accretionary skeletal carbonates—challenges and opportunities. *The Paleontological Society Papers* **18**, 133–166.
- Jenkyns H. C. (2010) Geochemistry of oceanic anoxic events. *Geochemistry, Geophysics, Geosystems* **11**. Available at: <http://agupubs.onlinelibrary.wiley.com/doi/abs/10.1029/2009GC002788> [Accessed July 8, 2020].
- Jennions, S. M., Thomas, E., Schmidt, D. N., Lunt, D., & Ridgwell, A. (2015). Changes in benthic ecosystems and ocean circulation in the Southeast Atlantic across Eocene Thermal Maximum 2. *Paleoceanography*, *30*(8), 1059-1077.



- 683 Jones A. M., Iacumin P. and Young E. D. (1999) High-resolution $\delta^{18}\text{O}$ analysis of tooth enamel phosphate by isotope ratio monitoring gas
684 chromatography mass spectrometry and ultraviolet laser fluorination. , 8.
685 Judd E. J., Wilkinson B. H. and Ivany L. C. (2018) The life and time of clams: Derivation of intra-annual growth rates from high-resolution oxygen
686 isotope profiles. *Palaeogeography, Palaeoclimatology, Palaeoecology* **490**, 70–83.
687 Kele S., Breitenbach S. F., Capezzuoli E., Meckler A. N., Ziegler M., Millán I. M., Kluge T., Deák J., Hanselmann K. and John C. M. (2015)
688 Temperature dependence of oxygen-and clumped isotope fractionation in carbonates: a study of travertines and tufas in the 6–95 C temperature
689 range. *Geochimica et Cosmochimica Acta* **168**, 172–192.
690 Kim S.-T. and O’Neil J. R. (1997) Equilibrium and nonequilibrium oxygen isotope effects in synthetic carbonates. *Geochimica et Cosmochimica*
691 *Acta* **61**, 3461–3475.
692 Kocken, I. J., Müller, I. A. and Ziegler, M.: Optimizing the Use of Carbonate Standards to Minimize Uncertainties in Clumped Isotope Data,
693 *Geochemistry, Geophysics, Geosystems*, 20(11), 5565–5577, doi:10.1029/2019GC008545, 2019.
694 Kohn, M.J., 2004. Comment: tooth enamel mineralization in ungulates: implications for recovering a primary isotopic time-series, by BH Passey
695 and TE Cerling (2002). *Geochimica et Cosmochimica Acta* **68**, 403–405.
696 Korte C. and Ullmann C. V. (2018) Permian strontium isotope stratigraphy. *Geological Society, London, Special Publications* **450**, 105–118.
697 Laurentano V., Littler K., Polling M., Zachos J. C. and Lourens L. J. (2015) Frequency, magnitude and character of hyperthermal events at the onset
698 of the Early Eocene Climatic Optimum. *Climate of the Past* **11**, 1313–1324.
699 Laurentano V., Zachos J. C. and Lourens L. J. (2018) Orbitally Paced Carbon and Deep-Sea Temperature Changes at the Peak of the Early Eocene
700 Climatic Optimum. *Paleoceanography and Paleoclimatology* **33**, 1050–1065.
701 Lear C. H., Bailey T. R., Pearson P. N., Coxall H. K. and Rosenthal Y. (2008) Cooling and ice growth across the Eocene-Oligocene transition.
702 *Geology* **36**, 251–254.
703 LeGrande A. N. and Schmidt G. A. (2006) Global gridded data set of the oxygen isotopic composition in seawater. *Geophysical research letters*
704 **33**.
705 Legros R., Balmain N. and Bonel G. (1986) Structure and composition of the mineral phase of periosteal bone. *Journal of chemical research.*
706 *Synopses*, 8–9.
707 Lisiecki L. E. and Raymo M. E. (2005) A Pliocene-Pleistocene stack of 57 globally distributed benthic $\delta^{18}\text{O}$ records. *Paleoceanography* **20**.
708 Available at: <http://agupubs.onlinelibrary.wiley.com/doi/abs/10.1029/2004PA001071> [Accessed March 31, 2020].
709 Lourens L. J., Becker J., Bintanja R., Hilgen F. J., Tuentner E., Van de Wal R. S. and Ziegler M. (2010) Linear and non-linear response of late
710 Neogene glacial cycles to obliquity forcing and implications for the Milankovitch theory. *Quaternary Science Reviews* **29**, 352–365.
711 Lourens L. J., Sluijs A., Kroon D., Zachos J. C., Thomas E., Röhl U., Bowles J. and Raffi I. (2005) Astronomical pacing of late Palaeocene to early
712 Eocene global warming events. *Nature* **435**, 1083–1087.
713 Liu Z., Pagani M., Zinniker D., DeConto R., Huber M., Brinkhuis H., Shah S. R., Leckie R. M. and Pearson A. (2009) Global cooling during the
714 Eocene-Oligocene climate transition. *Science* **323**, 1187–1190.
715 Luz B. and Kolodny Y. (1985) Oxygen isotope variations in phosphate of biogenic apatites, IV. Mammal teeth and bones. *Earth and Planetary*
716 *Science Letters* **75**, 29–36.
717 McArthur J. M., Howarth R. J. and Shields G. A. (2012) Strontium isotope stratigraphy. *The geologic time scale* **1**, 127–144.
718 Meckler A. N., Ziegler M., Millán M. I., Breitenbach S. F. and Bernasconi S. M. (2014) Long-term performance of the Kiel carbonate device with
719 a new correction scheme for clumped isotope measurements. *Rapid Communications in Mass Spectrometry* **28**, 1705–1715.
720 Merz B. and Thieken A. H. (2005) Separating natural and epistemic uncertainty in flood frequency analysis. *Journal of Hydrology* **309**, 114–132.
721 Meyers S. R. (2014) *Astrochron: An R package for astrochronology.*, <http://cran.r-project.org/package=astrochron>. Available at:
722 <http://scholar.google.com/scholar?cluster=14876361610707754388&hl=en&oi=scholar> [Accessed May 30, 2017].
723 Meyers S. R. (2019) Cyclostratigraphy and the problem of astrochronologic testing. *Earth-Science Reviews* **190**, 190–223.
724 Miyaji, T., Tanabe, K., Matsushima, Y., Sato, S., Yokoyama, Y. and Matsuzaki, H.: Response of daily and annual shell growth patterns of the
725 intertidal bivalve *Phacosoma japonicum* to Holocene coastal climate change in Japan, *Palaeogeography, Palaeoclimatology, Palaeoecology*,
726 **286**(3), 107–120, doi:10.1016/j.palaeo.2009.11.032, 2010.
727 Mook W. G. (1970) Stable carbon and oxygen isotopes of natural waters in the Netherlands. *Isotope hydrology* **1970**, 163–190.
728 Morgan V. and van Ommen T. D. (1997) Seasonality in late-Holocene climate from ice-core records. *The Holocene* **7**, 351–354.
729 Mosley-Thompson E., Thompson L. G., Dai J., Davis M. and Lin P. N. (1993) Climate of the last 500 years: High resolution ice core records.
730 *Quaternary Science Reviews* **12**, 419–430.
731 Müller I. A., Fernandez A., Radke J., van Dijk J., Bowen D., Schwieters J. and Bernasconi S. M. (2017) Carbonate clumped isotope analyses with
732 the long-integration dual-inlet (LIDI) workflow: scratching at the lower sample weight boundaries: LIDI as key for more precise analyses on
733 much less carbonate material. *Rapid Communications in Mass Spectrometry* **31**, 1057–1066.
734 Nohl T., Jarochovska E. and Munnecke A. (2018) Revealing the genesis of limestone-marl alternations: a taphonomic approach. *Palaios* **34**, 15–
735 31.
736 Noorbergen L. J., Abels H. A., Hilgen F. J., Robson B. E., Jong E. de, Dekkers M. J., Krijgsman W., Smit J., Collinson M. E. and Kuiper K. F.
737 (2018) Conceptual models for short-eccentricity-scale climate control on peat formation in a lower Palaeocene fluvial system, north-eastern
738 Montana (USA). *Sedimentology* **65**, 775–808.
739 Paillard D., Labeyrie L. D. and Yiou P. (1996) AnalySeries 1.0: a Macintosh software for the analysis of geophysical time-series. *Eos* **77**, 379.
740 Passey B. H. and Cerling T. E. (2002) Tooth enamel mineralization in ungulates: implications for recovering a primary isotopic time-series.
741 *Geochimica et Cosmochimica Acta* **66**, 3225–3234.
742 Pellegrini M. and Snoeck C. (2016) Comparing bioapatite carbonate pre-treatments for isotopic measurements: Part 2—Impact on carbon and
743 oxygen isotope compositions. *Chemical Geology* **420**, 88–96.
744 Petersen S. V., Tabor C. R., Lohmann K. C., Poulsen C. J., Meyer K. W., Carpenter S. J., Erickson J. M., Matsunaga K. K., Smith S. Y. and Sheldon
745 N. D. (2016) Temperature and salinity of the Late Cretaceous western interior seaway. *Geology* **44**, 903–906.
746 Philander S. G. H. (1983) El Niño southern oscillation phenomena. *Nature* **302**, 295–301.
747 R Core Team (2013) *R: A language and environment for statistical computing. R Foundation for Statistical Computing.*, Vienna, Austria. Available
748 at: <http://www.R-project.org/>.
749 Ramsey C. B. and Lee S. (2013) Recent and Planned Developments of the Program OxCal. *Radiocarbon* **55**, 720–730.
750 Rodríguez-Sanz L., Bernasconi S. M., Marino G., Heslop D., Müller I. A., Fernandez A., Grant K. M. and Rohling E. J. (2017) Penultimate deglacial
751 warming across the Mediterranean Sea revealed by clumped isotopes in foraminifera. *Scientific Reports* **7**, 1–11.
752 Rohling E. J. (2013) Oxygen isotope composition of seawater. *The Encyclopedia of Quaternary Science. Amsterdam: Elsevier* **2**, 915–922.



- 753 Saltzman M. R. and Thomas E. (2012) Carbon isotope stratigraphy. *The geologic time scale* **1**, 207–232.
754 Sano Y., Kobayashi S., Shirai K., Takahata N., Matsumoto K., Watanabe T., Sowa K. and Iwai K. (2012) Past daily light cycle recorded in the
755 strontium/calcium ratios of giant clam shells. *Nature Communications* **3**, 761.
756 Sato, S.: Temporal change of life-history traits in fossil bivalves: an example of *Phacosoma japonicum* from the Pleistocene of Japan,
757 *Palaeogeography, Palaeoclimatology, Palaeoecology*, 154(4), 313–323, doi:10.1016/S0031-0182(99)00106-6, 1999.
758 Schmitt J., Schneider R., Elsig J., Leuenberger D., Lourantou A., Chappellaz J., Kohler P., Joos F., Stocker T. F., Leuenberger M. and Fischer H.
759 (2012) Carbon Isotope Constraints on the Deglacial CO₂ Rise from Ice Cores. *Science* **336**, 711–714.
760 Scholz D. and Hoffmann D. L. (2011) StalAge—An algorithm designed for construction of speleothem age models. *Quaternary Geochronology* **6**,
761 369–382.
762 Schöne B. R. (2008) The curse of physiology—challenges and opportunities in the interpretation of geochemical data from mollusk shells. *Geo-*
763 *Marine Letters* **28**, 269–285.
764 Schöne B. R., Fiebig J., Pfeiffer M., Gleß R., Hickson J., Johnson A. L., Dreyer W. and Oschmann W. (2005) Climate records from a bivalved
765 *Methuselah* (*Arctica islandica*, Mollusca; Iceland). *Palaeogeography, Palaeoclimatology, Palaeoecology* **228**, 130–148.
766 Schöne B. R., Rodland D. L., Fiebig J., Oschmann W., Goodwin D., Flessa K. W. and Dettman D. (2006) Reliability of multitaxon, multiproxy
767 reconstructions of environmental conditions from accretionary biogenic skeletons. *The Journal of geology* **114**, 267–285.
768 Scourse, J., Richardson, C., Forsythe, G., Harris, I., Heinemeier, J., Fraser, N., Briffa, K. and Jones, P.: First cross-matched floating chronology
769 from the marine fossil record: data from growth lines of the long-lived bivalve mollusc *Arctica islandica*, The Holocene, 16(7), 967–974,
770 doi:10.1177/095968360606hl987rp, 2006.
771 Sha L., Mahata S., Duan P., Luz B., Zhang P., Baker J., Zong B., Ning Y., Brahim Y. A., Zhang H., Edwards R. L. and Cheng H. (2020) A novel
772 application of triple oxygen isotope ratios of speleothems. *Geochimica et Cosmochimica Acta* **270**, 360–378.
773 Shackleton N. J. (2000) The 100,000-Year Ice-Age Cycle Identified and Found to Lag Temperature, Carbon Dioxide, and Orbital Eccentricity.
774 *Science* **289**, 1897–1902.
775 Shao, D., Mei, Y., Yang, Z., Wang, Y., Yang, W., Gao, Y., Yang, L. and Sun, L. (2020) Holocene ENSO variability in the South China Sea recorded
776 by high-resolution oxygen isotope records from the shells of *Tridacna* spp., *Scientific Reports* **10** (1), 3921, doi:10.1038/s41598-020-61013-2.
777 Sinnesael M., De Vleeschouwer D., Zeeden C., Batenburg S. J., Da Silva A.-C., de Winter N. J., Dinarès-Turell J., Drury A. J., Gambacorta G. and
778 Hilgen F. J. (2019) The Cyclostratigraphy Intercomparison Project (CIP): consistency, merits and pitfalls. *Earth-Science Reviews*, 102965.
779 Sinnesael M., Zivanovic M., Vleeschouwer D. D., Claeys P. and Schoukens J. (2016) Astronomical component estimation (ACE v. 1) by time-
780 variant sinusoidal modeling. *Geoscientific Model Development*, 9, 3517–3531, 2016.
781 Stap L., Lourens L. J., Thomas E., Sluijs A., Bohaty S. and Zachos J. C. (2010) High-resolution deep-sea carbon and oxygen isotope records of
782 Eocene Thermal Maximum 2 and H2. *Geology* **38**, 607–610.
783 Steffensen J. P., Andersen K. K., Bigler M., Clausen H. B., Dahl-Jensen D., Fischer H., Goto-Azuma K., Hansson M., Johnsen S. J. and Jouzel J.
784 (2008) High-resolution Greenland ice core data show abrupt climate change happens in few years. *Science* **321**, 680–684.
785 Steuber T., Rauch M., Masse J.-P., Graaf J. and Malkoç M. (2005) Low-latitude seasonality of Cretaceous temperatures in warm and cold episodes.
786 *Nature* **437**, 1341–1344.
787 Straight W. H., Barrick R. E. and Eberth D. A. (2004) Reflections of surface water, seasonality and climate in stable oxygen isotopes from
788 tyrannosaurid tooth enamel. *Palaeogeography, Palaeoclimatology, Palaeoecology* **206**, 239–256.
789 Strauss J., Oleinik A. and Swart P. (2014) Stable isotope profiles from subtropical marine gastropods of the family Fasciolaridae: growth histories
790 and relationships to local environmental conditions. *Mar Biol* **161**, 1593–1602.
791 Surge D., Lohmann K. C. and Dettman D. L. (2001) Controls on isotopic chemistry of the American oyster, *Crassostrea virginica*: implications for
792 growth patterns. *Palaeogeography, Palaeoclimatology, Palaeoecology* **172**, 283–296.
793 Titschack J., Zuschin M., Spötl C. and Baal C. (2010) The giant oyster *Hytissia hyotis* from the northern Red Sea as a decadal-scale archive for
794 seasonal environmental fluctuations in coral reef habitats. *Coral Reefs* **29**, 1061–1075.
795 Treble P., Shelley J. M. G. and Chappell J. (2003) Comparison of high resolution sub-annual records of trace elements in a modern (1911–1992)
796 speleothem with instrumental climate data from southwest Australia. *Earth and Planetary Science Letters* **216**, 141–153.
797 Tsukakoshi Y. (2011) Sampling variability and uncertainty in total diet studies. *Analyst* **136**, 533–539.
798 Tudhope A. W. (2001) Variability in the El Niño-Southern Oscillation Through a Glacial-Interglacial Cycle. *Science* **291**, 1511–1517.
799 Ullmann C. V., Wiechert U. and Korte C. (2010) Oxygen isotope fluctuations in a modern North Sea oyster (*Crassostrea gigas*) compared with
800 annual variations in seawater temperature: Implications for palaeoclimate studies. *Chemical Geology* **277**, 160–166.
801 Van Rampelbergh M., Verheyden S., Allan M., Quinif Y., Keppens E. and Claeys P. (2014) Seasonal variations recorded in cave monitoring results
802 and a 10 year monthly resolved speleothem $\delta^{18}\text{O}$ and $\delta^{13}\text{C}$ record from the Han-sur-Lesse cave, Belgium. *Climate of the Past Discussions* **10**,
803 1821–1856.
804 Vansteenberghe S., Verheyden S., Cheng H., Edwards R. L., Keppens E. and Claeys P. (2016) Paleoclimate in continental northwestern Europe
805 during the Eemian and early Weichselian (125–97 ka): insights from a Belgian speleothem. *Clim. Past* **12**, 1445–1458.
806 Vansteenberghe S., Winter N. de, Sinnesael M., Verheyden S., Goderis S., Malderen S. J. M. V., Vanhaecke F. and Claeys P. (2019) Reconstructing
807 seasonality through stable isotope and trace element analysis of the Proserpine stalagmite, Han-sur-Lesse Cave, Belgium: indications for
808 climate-driven changes during the last 400 years. *Climate of the Past Discussions*, 1–32.
809 Veizer J. and Prokoph A. (2015) Temperatures and oxygen isotopic composition of Phanerozoic oceans. *Earth-Science Reviews* **146**, 92–104.
810 Vleeschouwer D. D., Vahlenkamp M., Crucifix M. and Pälike H. (2017) Alternating Southern and Northern Hemisphere climate response to
811 astronomical forcing during the past 35 m.y. *Geology* **45**, 375–378.
812 Wan R., Liu W., McArthur J. M. and Wang Z. (2019) Sr-isotope chronology of carbonate rocks: Quantifying the uncertainty of inversion. In
813 *Stratigraphy & Timescales* Elsevier. pp. 35–72. Available at: <https://linkinghub.elsevier.com/retrieve/pii/S2468517819300036> [Accessed June
814 17, 2020].
815 Warter V. and Müller W. (2017) Daily growth and tidal rhythms in Miocene and modern giant clams revealed via ultra-high resolution LA-ICPMS
816 analysis—A novel methodological approach towards improved sclerochemistry. *Palaeogeography, Palaeoclimatology, Palaeoecology* **465**,
817 362–375.
818 Wilkinson, B.H., Ivany, L.C., 2002. Paleoclimatic inference from stable isotope profiles of accretionary biogenic hardparts – a quantitative approach
819 to the evaluation of incomplete data. *Palaeogeography, Palaeoclimatology, Palaeoecology* **185**, 95–114. [https://doi.org/10.1016/S0031-](https://doi.org/10.1016/S0031-0182(02)00279-1)
820 [0182\(02\)00279-1](https://doi.org/10.1016/S0031-0182(02)00279-1)
821 Yan H., Liu C., An Z., Yang W., Yang Y., Huang P., Qiu S., Zhou P., Zhao N. and Fei H. (2020) Extreme weather events recorded by daily to
822 hourly resolution biogeochemical proxies of marine giant clam shells. *Proceedings of the National Academy of Sciences*.



- 823 Yobregat E., Fitoussi C. and Bourdon B. (2017) A new method for TIMS high precision analysis of Ba and Sr isotopes for cosmochemical studies.
824 *J. Anal. At. Spectrom.* **32**, 1388–1399.
825 Zachos J., Pagani M., Sloan L., Thomas E. and Billups K. (2001) Trends, rhythms, and aberrations in global climate 65 Ma to present. *Science* **292**,
826 686–693.
827 Zhang Limin, Tang Wilson H., Zhang Lulu and Zheng Jianguo (2004) Reducing Uncertainty of Prediction from Empirical Correlations. *Journal of*
828 *Geotechnical and Geoenvironmental Engineering* **130**, 526–534.